

Interleukin 17 signaling supports clinical benefit of dual CTLA-4 and PD-1 checkpoint inhibition in melanoma

Received: 22 October 2021

Accepted: 6 July 2023

Published online: 31 July 2023

 Check for updates

Renáta Váraljai¹ , Lisa Zimmer¹, Yahya Al-Matary¹, Paulien Kaptein², Lea J. Albrecht¹, Batool Shannan¹, Jan C. Brase³, Daniel Gusenleitner⁴, Teresa Amaral⁵, Nina Wyss⁶, Jochen Utikal^{7,8,9}, Lukas Flatz^{5,6}, Florian Rambow^{1,10}, Hans Christian Reinhardt^{11,12}, Jenny Dick¹³ , Daniel R. Engel¹³, Susanne Horn^{1,14}, Selma Ugurel¹, Wiebke Sondermann¹ , Elisabeth Livingstone¹, Antje Sucker¹, Annette Paschen¹ , Fang Zhao¹ , Jan M. Placke¹, Jasmin M. Klose¹⁵, Wolfgang P. Fendler¹⁵, Daniela S. Thommen¹ , Iris Helfrich^{1,16}, Dirk Schadendorf¹ ^{1,12,17} & Alexander Roesch¹ ^{1,12} 

Recent studies suggest that *BRAF*^{V600}-mutated melanomas in particular respond to dual anti-programmed cell death protein 1 (PD-1) and anti-cytotoxic T lymphocyte-associated protein 4 (CTLA-4) immune checkpoint inhibition (ICI). Here we identified an over-representation of interleukin (IL)-17–type 17 helper T (T_H17) gene expression signatures (GES) in *BRAF*^{V600}-mutated tumors. Moreover, high baseline IL-17 GES consistently predicted clinical responses in dual-ICI-treated patient cohorts but not in mono anti-CTLA-4 or anti-PD-1 ICI cohorts. High IL-17 GES corresponded to tumor infiltration with T cells and neutrophils. Accordingly, high neutrophil infiltration correlated with clinical response specifically to dual ICI, and tumor-associated neutrophils also showed strong IL-17–T_H17 pathway activity and T cell activation capacity. Both the blockade of IL-17A and the depletion of neutrophils impaired dual-ICI response and decreased T cell activation. Finally, high IL-17A levels in the blood of patients with melanoma indicated a higher global T_H17 cytokine profile preceding clinical response to dual ICI but not to anti-PD-1 monotherapy, suggesting a future role as a biomarker for patient stratification.

Treatment with immune checkpoint inhibition (ICI) has substantially improved survival of patients with metastatic melanoma (MM). Unfortunately, not all patients benefit to the same extent, as the majority relapses or experiences severe immune-related adverse events (irAEs). Still, there is a lack of feasible biomarkers and mechanistic understanding for risk stratification of patients with melanoma before ICI therapy. For example, in the CheckMate 067 study, treatment with the anti-PD-1 antibody nivolumab combined with the anti-CTLA-4

antibody ipilimumab ('dual ICI') showed a higher 6.5-year overall survival (OS) rate at 49% as opposed to 42% and 23% in the nivolumab and ipilimumab arms, respectively. The frequency of grade 3 and 4 toxicities was 59% with nivolumab plus ipilimumab, significantly higher than with nivolumab or ipilimumab alone (24% and 28%)¹.

However, one unexpected observation from this study was that patients with *BRAF*^{V600} mutations in the nivolumab plus ipilimumab group survived longer than *BRAF*-wild-type (WT) patients (6.5-year OS

rate of 57% versus 46%, median progression-free survival (PFS) of 16.8 versus 11.2 months). Interestingly, in the nivolumab and ipilimumab monotherapy arms, there were no or only small survival differences when stratified according to *BRAF* mutations^{1,2}. Accordingly, also in the IMMUNED trial, patients with *BRAF*^{V600} mutations benefited from nivolumab plus ipilimumab more than *BRAF*-WT patients (hazard ratio (HR) for risk of recurrence or death, 0.11 versus 0.44, $P = 0.019$)³. Thus, unraveling *BRAF*-associated immunological pathways may lead to better understanding of the biologic mediators of therapeutic response to dual ICI and could provide a rationale to stratify patient treatment upfront.

The IL-17 family includes six structurally relevant members (IL-17A–IL-17F) and is a pro-inflammatory cytokine produced by a subset of CD4⁺ T cells, primarily type 17 helper T (T_H17) cells^{4,5}, CD8⁺ T cells and various innate immune cell types⁶. Compelling evidence suggests that IL-17 has an essential role in a multitude of autoimmune diseases and inflammation⁷. While several reports suggest that particularly inflamed tumors respond better to ICI⁸, it is controversial whether T_H17–IL-17 inflammation could have an anti-tumor effect in melanoma, particularly during combined anti-PD-1 and anti-CTLA-4 therapy.

In this Article, it suggests that melanomas with pre-existent IL-17 signaling at therapy baseline benefit more from dual-ICI therapy. IL-17 signaling creates a favorable tumor microenvironment with increased immune infiltration, including neutrophils, and fosters T cell activation in preclinical melanoma mouse models and across different melanoma patient cohorts.

Results

The IL-17 pathway predicts clinical response to dual ICI

To find a molecular rationale for ICI therapy prediction in patients with melanoma based on the observed difference in response to dual ICI between *BRAF*-mutant and *BRAF*-WT melanomas, we performed gene expression profiling of treatment-naïve archived tumor samples (discovery set: $n = 77$ *BRAF*-mutant (V600 hotspot-positive), $n = 79$ *BRAF*-WT melanomas; Fig. 1a, left). To reveal GES in therapeutically relevant immune and resistance pathways, we applied NanoString technology due to its analytical robustness with optimized detection of low-expression RNA targets in formalin-fixed paraffin-embedded material. The baseline clinical characteristics of the discovery cohort and details on the NanoString gene panels have been recently described⁹. Differential gene expression analysis revealed diverging transcriptional landscapes between *BRAF*-mutant and *BRAF*-WT tumors. There were 21 transcripts significantly upregulated in *BRAF*-mutant tumors with enrichment for cytokine- and chemokine-encoding genes (Fig. 1a,b and Supplementary Table 1). In particular, we found transcriptional signatures indicative of interleukin signaling, especially IL-17, and associated T_H17 cell differentiation pathways being over-represented in *BRAF*-mutant tumors based on pathway enrichment and gene correlation analyses (Fig. 1b,c). In addition, gene set enrichment analysis

confirmed IL-17 GES upregulation in *BRAF*-mutant tumors (Extended Data Fig. 1a).

As it has been described that IL-17 signaling requires mitogen-activated protein kinase (MAPK) activation^{10,11}, we expanded our analyses to common oncogenic MAPK mutations beyond *BRAF*^{V600}. Both IL-17 and T_H17 cell differentiation GES were among the most significantly over-represented pathways in MAPK-mutated ($n = 77$ *BRAF* hotspot-mutant, $n = 42$ *NRAS* hotspot-mutant, $n = 1$ *NFI*-mutant) melanomas compared to triple-WT melanomas ($n = 36$) (Extended Data Fig. 1b). To further validate the link between IL-17 signaling GES (defined according to Kyoto Encyclopedia of Genes and Genomes (KEGG) hsa04657) and the MAPK pathway, we analyzed data from the largest available melanoma dataset from the Cancer Genome Atlas (TCGA) Skin Cutaneous Melanoma (TCGA-SKCM) cohort and found a significant association between IL-17 GES and the MAPK mutational state (Fig. 1d). Furthermore, this association was also significant when we correlated IL-17 GES with the transcriptional oncogenic activation signature of the MAPK pathway (MAPK-Pathway Responsive Genes (PROGENy)¹²; Fig. 1e).

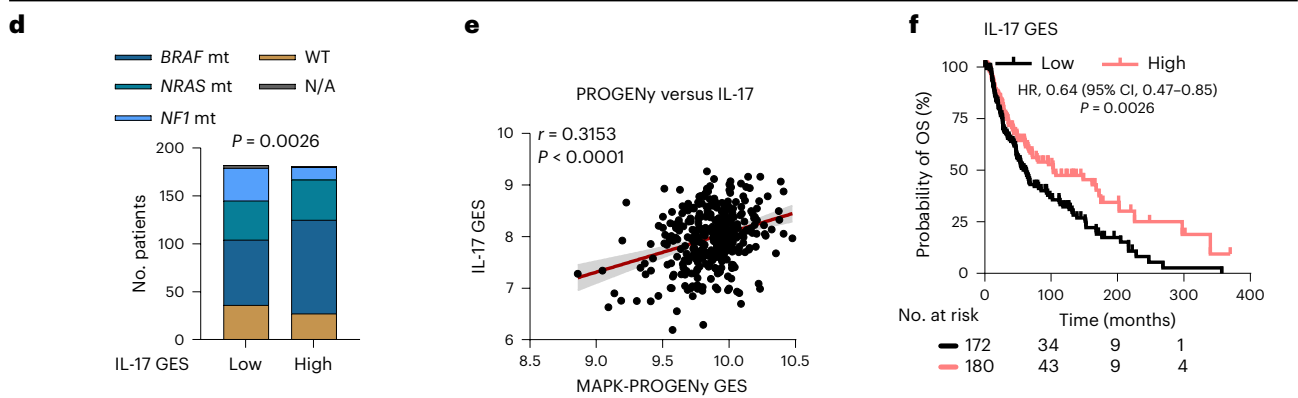
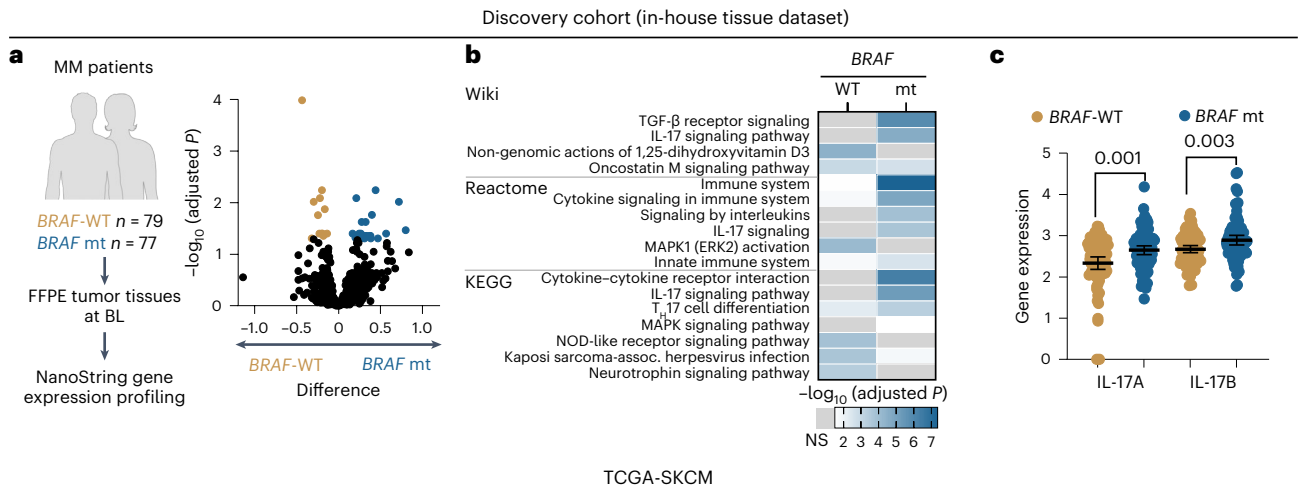
The MAPK pathway plays a role in cellular survival and proliferation, but it is also involved in the production and expression of pro-inflammatory cytokines. Therefore, we correlated the oncogenic activation of the MAPK pathway in melanoma cells with specific cytokines known to regulate IL-17 induction. We found that several IL-17-inducing genes were expressed at higher levels in *BRAF*-mutant than in *BRAF*-WT tumors in the SKCM cohort and that their expression was significantly decreased in MAPK inhibitor (MAPKi)-treated melanoma tissue biopsies^{13–15} (Extended Data Fig. 1c,d). To further confirm the regulatory axis between MAPK activation and IL-17 regulators, we demonstrated, by pharmacologic manipulation in vitro, that IL-17-inducing genes can be expressed by *BRAF*-mutant melanoma cells themselves, and dual MAPKi (dabrafenib plus trametinib) leads to decreased transcription of IL-17-regulatory genes (Extended Data Fig. 1e).

To investigate a potentially relevant prognostic value of baseline IL-17 GES in melanoma tissues that is universal and not necessarily dependent only on MAPK signaling, we explored the association between OS and IL-17 signaling in the TCGA-SKCM dataset that mainly consists of untreated melanoma tumors. Indeed, high IL-17 GES was significantly associated with improved OS (HR, 0.64; 95% confidence interval (CI), 0.47–0.85; $P = 0.0026$; Fig. 1f). Next, we analyzed four different RNA-seq datasets from ICI-treated patient cohorts with MM of various genotypes (combined cohorts of anti-CTLA-4, anti-PD-1 or anti-CTLA-4 and anti-PD-1 therapy; Van Allen et al., Liu et al., Riaz et al. and Gide et al.; exact patient numbers are provided in the Methods)^{16–19}. Intriguingly, high expression of core IL-17 signaling genes (IL-17A–IL-17F GES; IL-17 family cytokines containing the six structurally related cytokines) predicted longer PFS in dual-ICI-treated patients (HR, 0.45; 95% CI, 0.26–0.79; $P = 0.0057$), while it did not correlate with treatment response to anti-PD-1 or anti-CTLA-4 monotherapy (Fig. 1g–i).

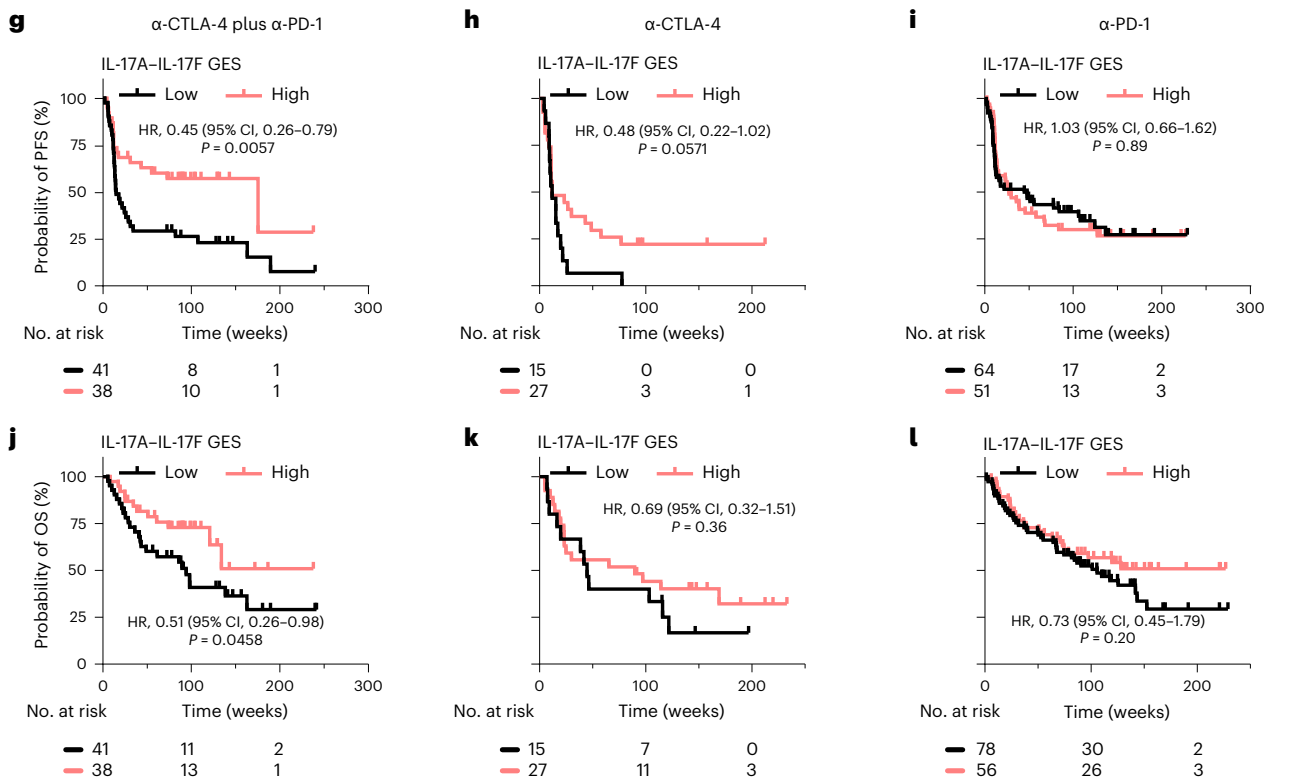
Fig. 1 | IL-17 pathway genes are associated with improved response to dual ICI.

a, Left, schematic representation of the discovery cohort. Right, volcano plot showing the difference in *BRAF*-WT ($n = 79$ V600-negative samples)- and *BRAF*-mutant ($n = 77$ V600-positive samples)-associated gene expression (\log_2 (values)) and q values ($-\log_{10}$ (adjusted P values)) from multiple unpaired t -tests with Benjamini, Krieger and Yekutieli test correction) in the discovery cohort. Each dot represents a gene; significant differentially expressed genes ($q < 0.05$) are shown in a color-coded manner. **b**, Heatmap showing enrichment scores ($-\log_{10}$ (adjusted P values), Benjamini–Hochberg-corrected FDR) of functional pathways in Wiki, Reactome and KEGG pathway databases. **c**, Scatter dot plots showing gene expression of *IL17A* and *IL17B* ($n = 79$ *BRAF*-WT, $n = 77$ *BRAF*-mutant tumors). Dots represent biologically independent patient samples. Mean \pm 95% CIs are plotted; P values are from the unpaired t -test. **d**, Stacked bar plot showing the number of patients according to IL-17 signaling GES (according to KEGG hsa04657; cut point

at median) and mutational subgroups in the TCGA-SKCM cohort ($n = 363$ tumor tissues). The P value is from the χ^2 test. **e**, Scatterplot showing the correlation between IL-17 and the PROGENy MAPK activation GES in the TCGA-SKCM cohort ($n = 363$ tumor tissues). The line is from linear regression \pm 95% CI bands. **f**, Kaplan–Meier plot for OS according to the IL-17 signaling GES (KEGG hsa04657) in the TCGA-SKCM cohort. **g–i**, Kaplan–Meier plots for PFS (**g–i**) and OS (**j–l**) according to the IL-17 family GES (IL-17A–IL-17F GES; IL-17 family cytokines containing the six structurally related cytokines) in patients treated with dual-ICI (**g,j**), mono anti-CTLA-4 (**h,k**) and mono anti-PD-1 (**i,l**) therapy. **g–l**, HR and 95% CIs are reported for high-expression groups. P values were calculated with the log-rank test. Categorization into ‘high’ versus ‘low’ was done according to an optimal cut point. All P values are two tailed. mt, mutant; FFPE, formalin fixed, paraffin embedded; BL, baseline; NS, not significant; NOD, nucleotide-binding oligomerization domain; assoc., associated; α , anti; N/A, not available.



ICI cohorts (Gide et al.¹⁸, Riaz et al.¹⁹, Liu et al.¹⁷, Van Allen et al.¹⁶)



High IL-17 signaling was also associated with longer OS in dual ICI (HR, 0.51; 95% CI, 0.26–0.98; $P = 0.0458$) but not in ICI monotherapies (Fig. 1j–l).

Overall, these results suggest co-regulation of the IL-17 and the MAPK pathway, particularly in *BRAF*-mutant melanomas in which there is strong MAPK activation. However, IL-17 pathway activity is probably not restricted to (known) oncogenic MAPK activators and may instead be a universal predictor of response to ICI.

IL-17A is crucial for response to dual ICI in mouse melanoma

To study the effect of the systemic IL-17A level on the anti-tumor efficacy of ICI therapy in vivo, we used two syngeneic melanoma transplantation models with distinct genotypes and response profiles to experimentally administered anti-CTLA-4 and anti-PD-1 antibodies^{20,21}. First, we examined the effects of an IL-17A-neutralizing antibody (α -IL-17A) and recombinant mouse IL-17A (rm-IL-17A) on tumor growth kinetics in the ICI-sensitive MT/*ret*-derived primary cutaneous melanoma (CM) mouse model (human *ret* transgene, *BRAF*-WT²⁰). As expected, dual ICI significantly slowed down CM tumor growth compared to controls ($P = 0.0172$). Treatment with dual ICI in combination with rm-IL-17A also decreased tumor growth ($P = 0.0073$ versus controls), whereas the addition of α -IL-17A strongly blocked the anti-tumor effect of dual ICI ($P = 0.0130$ versus dual ICI; Fig. 2a) and significantly shortened survival (Extended Data Fig. 2a). Endpoint analysis of serum IL-17A levels confirmed that the addition of α -IL-17A resulted in significantly less serum IL-17A than levels from dual-ICI-treated mice ($P = 0.0109$; Fig. 2b). Furthermore, we found a negative correlation between tumor size and serum IL-17A levels, with especially large aggressive tumors (≥ 800 mm³) having significantly lower IL-17A concentrations ($P = 0.0155$; Fig. 2c).

To understand whether IL-17A is also a relevant contributor to CTLA-4 and PD-1 blockade in human melanomas, we used an ex vivo patient-derived tumor fragment (PDTF) model, which has recently demonstrated high predictive capacity for ICI^{22,23}. PDTFs from three ICI-responsive patient melanomas were treated with dual ICI in the absence or presence of α -IL-17A. In line with the effects observed in mouse models, α -IL-17A decreased immune activation upon dual ICI and particularly abrogated IFN- γ -induced responses, which is known as a critical driver of clinical response to ICI²⁴ (Fig. 2d–f).

Next, we characterized the tumor microenvironment to unravel the landscape of IL-17-mediated early immune cell infiltration. We set up a short-term treatment regimen in the CM model (using the same drug doses) and performed multiplex immunofluorescence staining. Overall, tumors treated with dual ICI alone or in combination with rm-IL-17A had higher immune cell infiltration than the control. In particular, CD8⁺ T cells that are the main effectors of therapeutic ICI²⁵ were increased in tumors treated with dual ICI alone or in combination with rm-IL-17A. Furthermore, CD4⁺ cells, IL-17A⁺ cells, CD11c⁺ cells and Ly6G⁺ neutrophils that are potential downstream effectors of IL-17 functions were also significantly enriched in tumors treated with dual ICI alone or in combination with rm-IL-17A, whereas the addition of α -IL-17A

counteracted the effect of dual ICI and prevented immune cell infiltration (Fig. 2g and Extended Data Fig. 2b).

Second, we asked whether IL-17 could improve ICI responsiveness also in an intrinsically resistant tumor scenario and applied the YUMML7 mouse model, which was reported to lack response to ICI (*Pten*^{del}, *Cdkn2a*^{del}, *BRAT*^{V600E}-mutant melanoma²¹). As expected, YUMML7 tumors treated with dual ICI showed no response, and mice developed tumors similar to the control ($P > 0.05$ versus control). However, addition of rm-IL-17A significantly slowed down tumor growth ($P = 0.0487$ versus control, $P = 0.0016$ versus dual ICI; Extended Data Fig. 2c). Endpoint analysis of serum samples revealed that addition of rm-IL-17A to dual ICI resulted in increased production of the T cell chemokines IFN- γ , CXCL9 and CXCL10, which have been shown to play a role in ICI response and CD8⁺ T cell recruitment²⁶ (Extended Data Fig. 2d). Together, these findings indicated that increased IL-17 signaling contributes to better response in dual ICI.

The IL-17-associated cellular microenvironment in dual ICI

In silico analysis of different bulk RNA-seq datasets showed that high IL-17 expression is positively correlated with high presence of T_H17 cells and T cells, dendritic cells, mast cells and neutrophils (Fig. 3a). Notably, IL-17-associated elevation of T_H17 cells, dendritic cells and neutrophils is already present in untreated tumors (TCGA-SKCM data), suggesting that subgroups of melanomas harbor a pre-existent immune composition that may determine susceptibility to dual ICI upfront to therapy.

IL-17 is known to activate innate immune mechanisms by inducing expression of pro-inflammatory cytokines and recruitment of neutrophils⁴. Accordingly, we found that neutrophil gene signatures are significantly enriched in baseline tumors of dual-ICI responders ($P = 0.0136$) but not in mono anti-PD-1 responders ($P = 0.2109$, Gide et al. dataset¹⁸; Fig. 3b). Moreover, high neutrophil abundance at baseline correlated with longer PFS (HR, 0.19; 95% CI, 0.05–0.70; $P = 0.0123$) in the dual-ICI cohort (Fig. 3c).

To experimentally validate the role of neutrophils in response to ICI, we injected C57BL/6N mice either with ICI-sensitive MT/*ret* CM cells or the ICI-resistant MT/*ret* LN subline (derived from a single resistant lymph node²⁰; Extended Data Fig. 3a) and expanded the tumors to a size of ~250 mm³. We then isolated tumor-associated neutrophils (TANs) from both models and performed liquid chromatography-mass spectrometry/mass spectrometry (LC-MS/MS) (Fig. 3d). We analyzed the differentially expressed proteins and enriched functional pathways between ICI-sensitive and ICI-resistant TANs and found a significantly higher expression of proteins belonging to DNA replication, ribosome and the IL-17 signaling pathway in ICI-sensitive TANs (Fig. 3e). Next, we isolated naive bone marrow (BM) neutrophils from C57BL/6N mice and cultured them in conditioned medium derived from ICI-sensitive CM melanoma cells with or without α -IL-17A for 24 h (Fig. 3f). We confirmed that several IL-17 signaling genes were expressed at a significantly higher level in BM neutrophils stimulated with conditioned medium from intrinsically ICI-sensitive mouse melanoma and that this was abrogated by

Fig. 2 | IL-17A supports anti-tumor effects of dual ICI. a, Tumor growth kinetics of transplanted CM (*BRAF*-WT ICI-sensitive) melanoma tumors treated with immunoglobulin G (IgG) or H₂O (control, $n = 6$), anti-CTLA-4 + anti-PD-1 ($n = 6$), anti-CTLA-4 + anti-PD-1 + rm-IL-17A ($n = 6$) and anti-CTLA-4 + anti-PD-1 + α -IL-17A ($n = 6$) antibodies according to the depicted treatment schedule. Data points show mean + s.e.m. until the day when the first mice were eliminated from each group; P values are from one-way ANOVA with Tukey's multiple-comparison test. **b**, Serum IL-17A levels from the endpoint measurement (day 33) by ELISA. Shown are mean + s.e.m. of $n = 3$ –5 biologically independent samples per group; P values are from one-way ANOVA with Holm–Sidak's multiple-comparison test. **c**, Corresponding serum IL-17A levels in mice grouped according to final tumor volume ($n = 6$ (<800 mm³) versus $n = 10$ (≥ 800 mm³) biologically independent samples). The bar plot shows mean + s.e.m., and the P value is from an unpaired

t -test. **d, e**, Heatmap (**d**) and corresponding x - y plot (**e**) with z scores representing the normalized delta (stimulated – unstimulated condition) values of soluble mediators secreted by PDTFs from $n = 3$ human melanoma tumors treated ex vivo with anti-CTLA-4 + anti-PD-1 or with anti-CTLA-4 + anti-PD-1 + α -IL-17A antibodies. **f**, Delta values of IFN- γ , CXCL10 and CXCL9 secreted by PDTFs upon either anti-CTLA-4 + anti-PD-1 or anti-CTLA-4 + anti-PD-1 + α -IL-17A ex vivo treatment. **g**, Representative immunostaining images of CM tumors (day 9) showing melanoma (melan A) and immune cell markers (CD8a, CD11c, Ly6G). Scatter dot plots show the relative contribution of immune cells ($n = 5$ random fields per whole-tumor area, normalized to 4,6-diamidino-2-phenylindole (DAPI) values; $n = 2$ biologically independent tumors per group). All P values are two tailed. S, sensitive; s.c., subcutaneous; ♀, female; MEL, melanoma; CCL, C–C motif chemokine ligand; TNF, tumor necrosis factor.

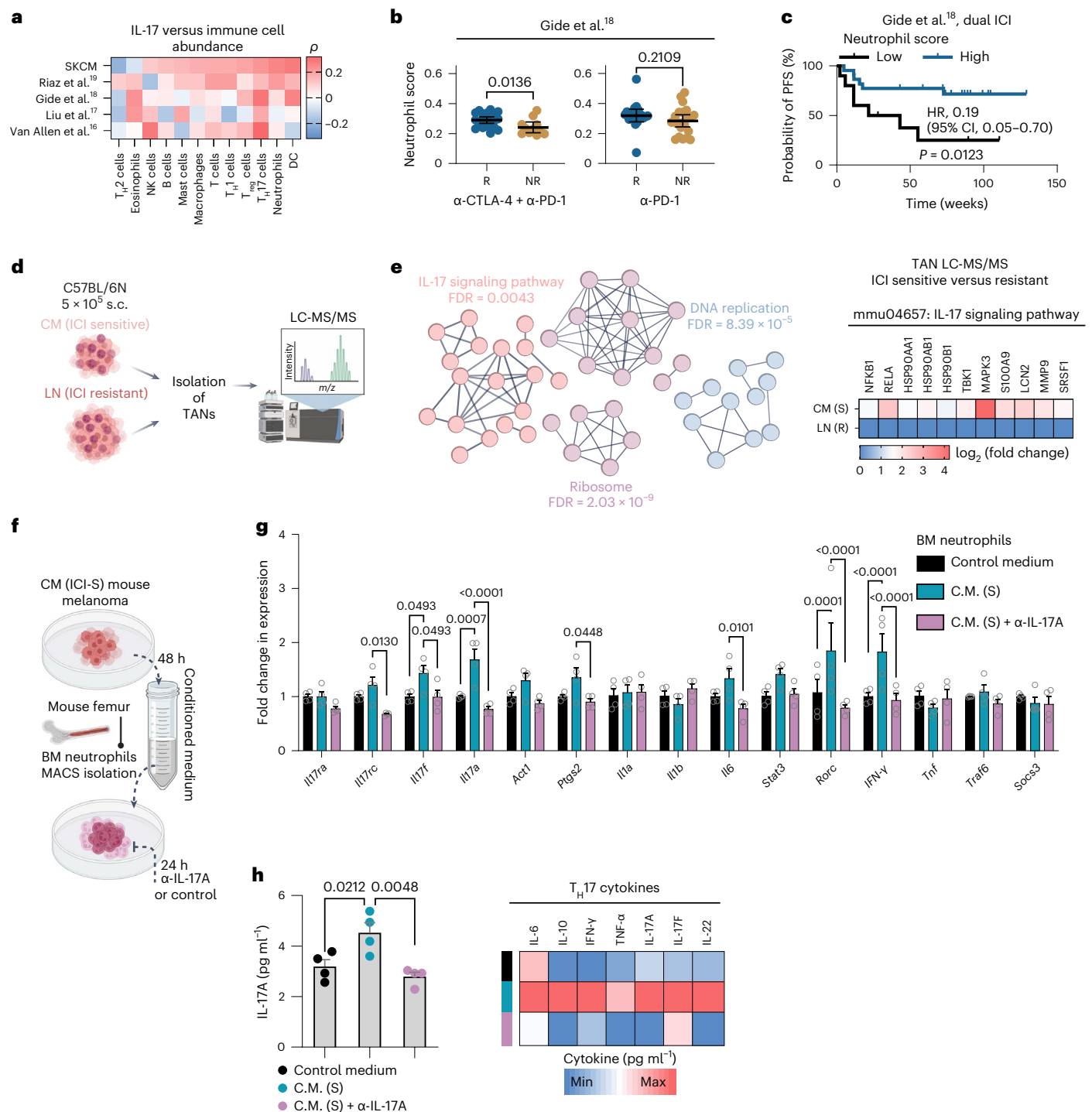
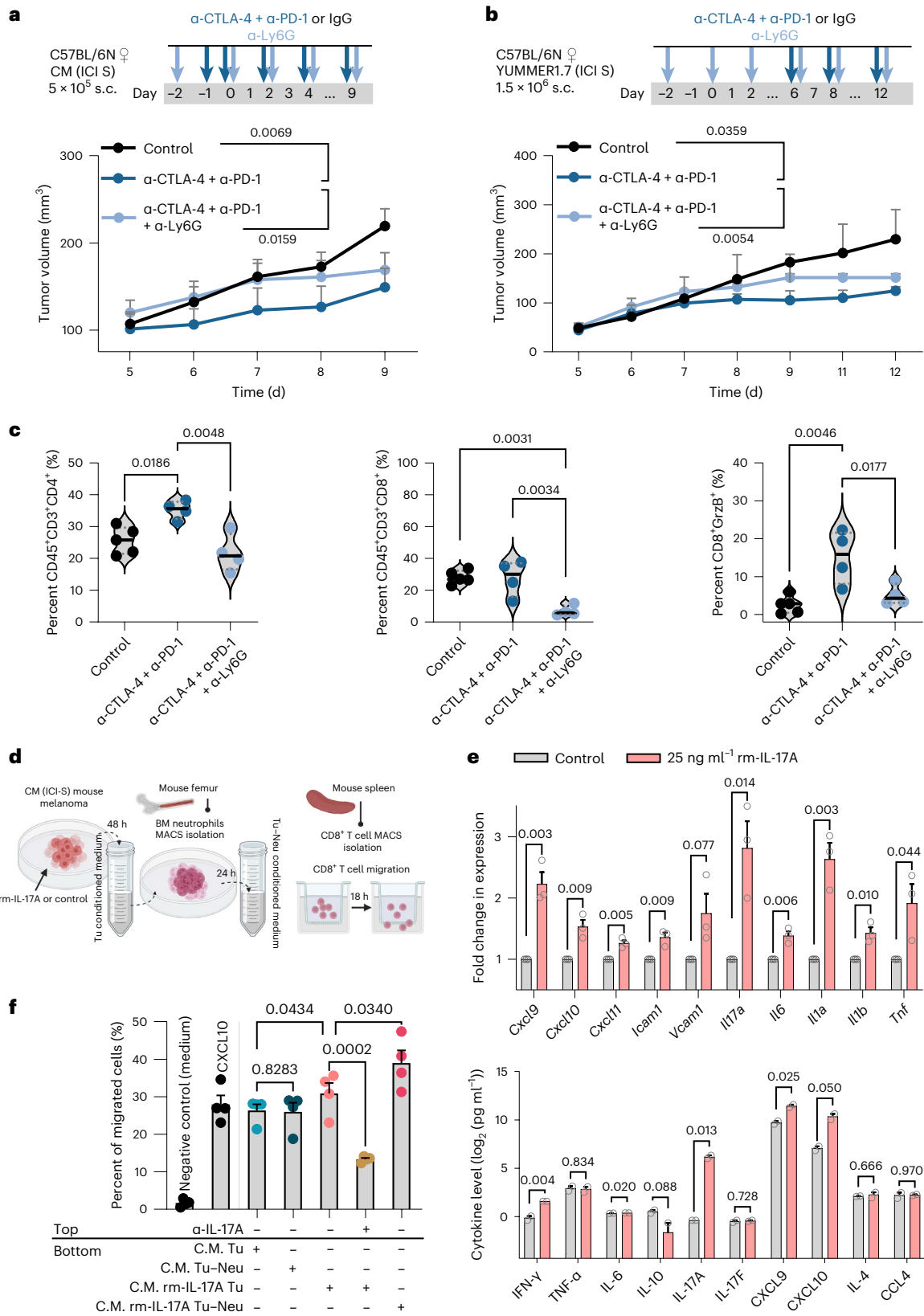


Fig. 3 | The IL-17 signaling-associated cellular microenvironment in melanomas treated with ICI. **a**, Heatmap showing Spearman correlation between immune cell types (following the Bindea et al.²³ algorithm) and IL-17A–IL-17F GES in tumor samples in bulk RNA-seq cohorts. **b**, Scatter dot plots showing estimated neutrophil cell enrichment in baseline tissue samples of therapy responders (*n* = 21) versus non-responders (*n* = 11) treated with dual ICI (left) and therapy responders (*n* = 19) versus non-responders (*n* = 22) treated with anti-PD-1 monotherapy (right) in the Gide et al.¹⁸ dataset. *P* values are from unpaired *t*-tests, and mean ± 95% CIs are plotted. Each dot represents a biologically independent sample. **c**, Kaplan–Meier plot for PFS according to baseline neutrophil cell enrichment levels (*n* = 10, ‘low’; *n* = 22, ‘high’, according to an optimal cut point) in the dual-ICI group of Gide et al.¹⁸. HRs and 95% CIs are reported for high-expression groups, and the *P* value is from the log-rank test. **d**, **e**, Schematic workflow (**d**) for LC-MS/MS analysis (**e**). LC/MS/MS icon created by [BioRender.com](#). Search Tool for the Retrieval of Interacting Genes/Proteins (STRING) analysis showing the top significantly enriched cellular pathways in TANs derived from

CM tumors. The corresponding heatmap shows fold change in protein expression of IL-17 signaling pathway (according to KEGG mmu04657) components. **f**, Schematic workflow for naive BM neutrophil isolation and in vitro analysis. **g**, Quantitative PCR (qPCR) analysis of key IL-17 signaling components in untreated versus α-IL-17A-treated (5 μg ml⁻¹) naive BM neutrophils cultured for 24 h in conditioned medium derived from CM mouse melanoma. Regular growth medium (no exposure to tumor cells) was used as a control. Bar plots represent mean ± s.e.m. from *n* = 4 biologically independent samples; *P* values are from two-way ANOVA with Holm–Sidak’s multiple-comparison test. Shown is one representative of three independently performed experiments. **h**, Corresponding IL-17A (left, bar plot) and T_H17 cytokine levels (right, heatmap) in the supernatants of BM neutrophils from **g**. The bar plot shows mean ± s.e.m.; dots represent individual biological replicates. *P* values are from one-way ANOVA with Sidak’s multiple-comparison test. C.M., conditioned medium; R, responder; NR, non-responder; DC, dendritic cell; MACS, magnetic-activated cell sorting; max, maximum; min, minimum; T_H, helper T cell; T_{reg}, regulatory T cell.



ICI-sensitive transplantation models (CM and YUMMER1.7). To avoid regeneration and expansion of BM neutrophils, we monitored short-term tumor growth kinetics. We verified that neutrophil depletion with the anti-Ly6G antibody technically worked in both models, evident by the reduced frequency of CD45⁺CD11b⁺Ly6G⁺ cells in blood, spleen and tumor samples collected at day 9 and day 12

(CM and YUMMER1.7 models, respectively; Extended Data Fig. 3c). Addition of the anti-Ly6G antibody to anti-CTLA-4 and anti-PD-1 antibodies significantly accelerated tumor growth and weakened the dual-ICI response in both models (Fig. 4a,b). Furthermore, flow cytometry analysis of intratumoral immune cell frequencies indicated that the increase in CD4⁺ and CD8⁺ T cells in dual-ICI-treated tumors was

Fig. 4 | The IL-17-associated presence of neutrophils plays a role in the anti-tumor response to dual ICI. Tumor growth kinetics of CM (*BRAF*-WT ICI-sensitive) (a) and YUMMER1.7 (*BRAF*-mutant ICI-sensitive) (b) tumors treated with IgG or H₂O (control, CM, *n* = 5; YUMMER1.7, *n* = 4), anti-CTLA-4 + anti-PD-1 antibodies (CM, *n* = 4; YUMMER1.7, *n* = 4) or anti-CTLA-4 + anti-PD-1 + anti-Ly6G antibodies (CM, *n* = 5; YUMMER1.7, *n* = 4) according to the depicted treatment schedule. Data points show mean + s.e.m.; *P* values are from one-way ANOVA with Holm–Sidak’s multiple-comparison test. c, Violin plots showing tumor immune cell frequencies by flow cytometry from a (CM model). *P* values are from one-way ANOVA with Holm–Sidak’s multiple-comparison test. d, Schematic workflow for in vitro culture, isolation of BM neutrophils and splenic CD8⁺ T cells followed by the migration assay. e, Top, qPCR analysis of transcripts encoding T cell chemokines, adhesion molecules and T_H17 signaling components in the control or rm-IL-17A-treated CM mouse cell line. Bar plots represent mean + s.e.m. from *n* = 3 biological

replicates; *P* values are from the unpaired *t*-test. Shown is one representative of two independently performed experiments. Bottom, corresponding cytokine and chemokine levels in cell culture supernatants of CM cells treated with rm-IL-17A. Data points show mean + s.e.m. from *n* = 2 biologically independent samples; *P* values are from the unpaired *t*-test. f, Bar plot showing the percentage of migrated CD8⁺ T cells in the Boyden chamber assay. The different medium conditions used as chemoattractant in the bottom chamber are depicted below the horizontal line. Serum-free medium was used as the negative control, and recombinant mouse CXCL10 (200 ng ml⁻¹) was used as the positive control. α-IL-17A (5 μg ml⁻¹) was added to the top chamber (depicted above the horizontal line) as indicated. Individual data points represent *n* = 3–4 biological replicates per group; *P* values are from one-way ANOVA with Sidak’s multiple-comparison test. Shown is one representative of three independently performed experiments. All *P* values are two tailed. Tu, tumor; Neu, neutrophil; Grz, granzyme.

counteracted by the anti-Ly6G antibody and that the frequency of intratumoral cytotoxic CD8⁺ T cells (CD8⁺granzyme B⁺ cell fraction) was significantly reduced in a neutrophil-lacking tumor microenvironment (Fig. 4c).

Because these results indicated possible crosstalk between TANs and cytotoxic mediators of the ICI response, we set up in vitro experiments to study the migration capacity of murine CD8⁺ T cells. We first generated conditioned medium from untreated and rm-IL-17A-treated ICI-sensitive CM mouse melanoma cells (tumor conditioned medium). In subsequent steps, the tumor cell-derived conditioned medium was used to culture naive BM neutrophils. After 24 h of culturing, the conditioned medium from the neutrophils was also collected (tumor neutrophil conditioned medium) and used as chemoattractant in CD8⁺ T cell migration Boyden chamber assays (Fig. 4d). Treatment with rm-IL-17A led to increased mRNA expression of key T cell chemokines such as CXCL9–CXCL11, adhesion molecules ICAM1 and VCAM1 and IL-17-dependent cytokines in melanoma cells. The corresponding cell culture supernatants also showed a significant increase in T cell chemokines and T_H17 cytokines (Fig. 4e). Consequently, conditioned medium from rm-IL-17A-treated melanoma cells attracted more CD8⁺ T cells than conditioned medium from untreated cells (*P* = 0.0434). Importantly, migration was significantly reduced by concurrent α-IL-17A treatment of CD8⁺ T cells (*P* = 0.0002; Fig. 4f). Finally, CD8⁺ T cell migration was increased when we used conditioned medium from tumor neutrophils treated with rm-IL-17A as compared to conditioned medium from rm-IL-17A-treated melanoma cells alone (*P* = 0.0340), while CD8⁺ T cell migration remained at a similar level when conditioned media from untreated melanoma cells versus untreated tumor neutrophils were used (*P* = 0.8283; Fig. 4f).

Overall, these results suggest that, in dual-ICI-sensitive melanoma, a tumor baseline scenario characterized by high IL-17 pathway activity and neutrophil accumulation positively stimulates T cell migration and tumor elimination.

Fig. 5 | IL-17A–T_H17 profiling for response prediction in ICI-treated patients with melanoma. a, Dual-ICI-treated melanoma patient cohort (first-line anti-CTLA-4 and anti-PD-1 therapy, *n* = 70). b, Plasma IL-17A levels as measured by ELISA in correlation to the best clinical response in samples collected at therapy baseline (*n* = 41 responders versus *n* = 29 non-responders) and at early follow-up (*n* = 33 responders versus *n* = 12 non-responders) visits. c, Kaplan–Meier plot for PFS according to the baseline IL-17A concentration. d, Heatmaps representing the median cytokine concentrations as quantified by multiplex cytokine array for responding versus non-responding patients. e, Corresponding volcano plot showing the effect size (Hedge’s *g*) and $-\log_{10}$ (*P* values) (Mann–Whitney *U*-test) for each cytokine for responding versus non-responding patients. f, Mono anti-PD-1-treated melanoma patient cohort (first-line anti-PD-1 therapy, *n* = 51). g, Plasma IL-17A levels as measured by ELISA in correlation to the best clinical response in samples collected at baseline (*n* = 19 responders versus *n* = 32 non-responders) and at early follow-up (*n* = 11 responders versus *n* = 14

IL-17A and T_H17 cytokines predict the response to dual ICI

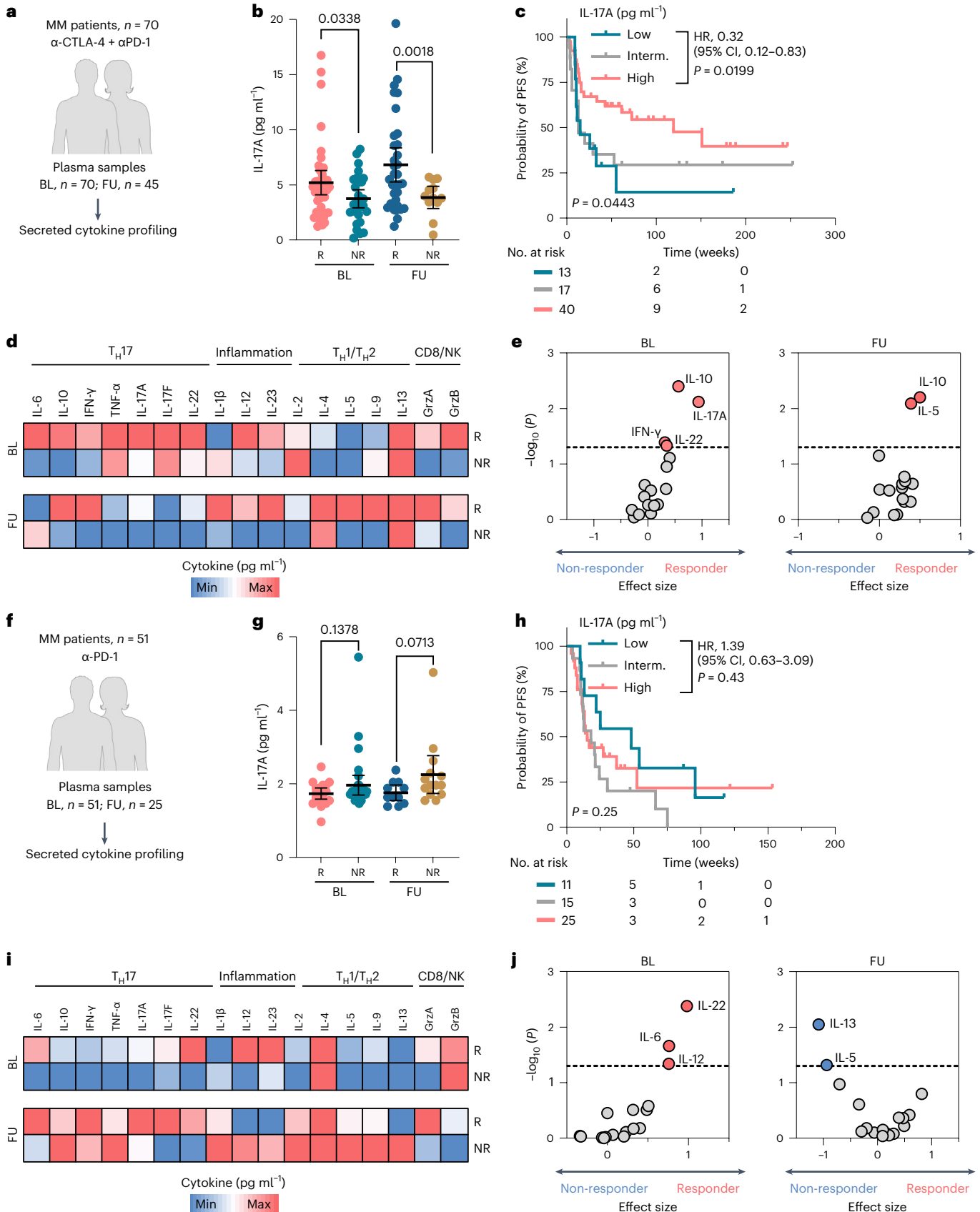
Our findings indicated thus far that IL-17 contributes to enhanced dual-ICI response and could serve as a therapy stratification biomarker. Therefore, we analyzed plasma samples of 121 patients with melanoma treated at the Essen Department of Dermatology with either first-line dual ICI (anti-CTLA-4 plus anti-PD-1 antibodies, *n* = 70) or with first-line anti-PD-1 monotherapy (*n* = 51) (Fig. 5a,f). Secreted IL-17A levels in samples collected at therapy baseline and also at early follow-up visits (median, week 9; range, 2–12 weeks) were significantly higher in therapy responders under dual-ICI treatment than in non-responders (*P* = 0.0338 at baseline, *P* = 0.0018 at follow-up; Fig. 5b). To test whether baseline IL-17A levels could be used as a biomarker for pre-therapeutic therapy stratification, we categorized patients according to their baseline IL-17A plasma concentrations. We applied the bioinformatic tool X-tile to achieve the optimal cut-point-based prognostication²⁸. We found that dual-ICI-treated patients with a high baseline IL-17A concentration (≥ 3.76 pg ml⁻¹) had longer PFS than patients with intermediate (2.30–3.75 pg ml⁻¹; *P* = 0.0682; HR, 0.46) or low (≤ 2.29 pg ml⁻¹; *P* = 0.0199; HR, 0.32) baseline IL-17A levels (Fig. 5c). To test whether elevated IL-17A is indicative of a global T_H17 cytokine profile and phenotype induction, we applied a bead-based multiplex cytokine array including several known T_H17, type 1 and 2 helper T cell, inflammatory and CD8⁺ T cell–natural killer (NK) (CD8/NK) activation-associated cytokines. Interestingly, dual-ICI therapy responders had higher T_H17-associated cytokine (IL-10, IFN-γ, IL-17A and IL-22; *P* < 0.05) levels, particularly at baseline (Fig. 5d,e). While other inflammatory and CD8/NK cytokines were also elevated in baseline and follow-up samples from responders, they did not statistically stratify patients (Fig. 5d,e).

By contrast, response to anti-PD-1 monotherapy showed no statistically significant correlation with the plasma IL-17A level, although there was a non-significant trend for elevated IL-17 levels in non-responders (Fig. 5f–h). Analysis of additional cytokines in the mono anti-PD-1 cohort revealed differences between therapy responders versus

non-responders) visits. h, Kaplan–Meier plot for PFS according to the baseline IL-17A concentration. i, Heatmaps representing median cytokine concentrations as quantified by multiplex cytokine array for responding versus non-responding patients. j, Corresponding volcano plot showing the effect size (Hedge’s *g*) and $-\log_{10}$ (*P* values) (Mann–Whitney *U*-test) for each cytokine for responding versus non-responding patients. *P* values are from the unpaired *t*-test with Welch’s correction, and mean ± 95% CIs are plotted in b,g. Each dot represents a biologically independent sample. Categorization into ‘high’ versus ‘low’ according to the X-tile-determined cut-point value was carried out separately within each dataset. HRs and 95% CIs are reported for ‘IL-17A high’, and *P* values are from the log-rank test in c,h. Significant predictors of response or non-response are shown above the dashed line (*P* < 0.05) in baseline or follow-up plasma samples in e,j. All *P* values are two tailed. FU, follow-up; responder, complete and partial responses; non-responder, progressive disease, mixed response; interm., intermediate.

non-responders to a lesser extent, with only baseline IL-6, IL-22 and IL-12 ($P < 0.05$) significantly stratifying patients according to response. Interestingly, and in contrast to dual-ICI responders, T_H17

cytokines were higher in mono anti-PD-1 responders at follow-up but not in baseline plasma samples (statistically not significant, $P = 0.5781$; Fig. 5i,j).



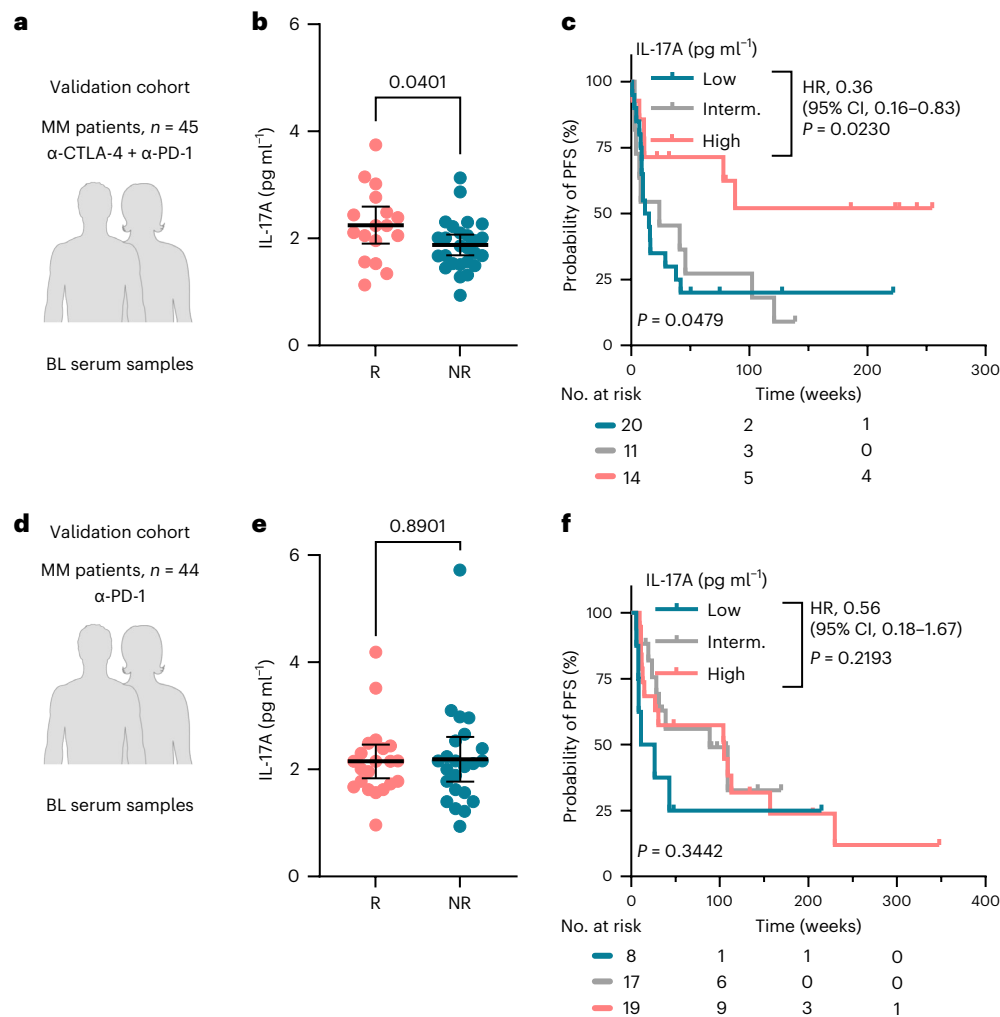


Fig. 6 | Validation cohort. **a**, Dual-ICI-treated melanoma validation cohort (anti-CTLA-4 and anti-PD-1 antibodies, $n = 45$). **b**, Serum IL-17A levels as measured by ELISA in correlation to the best clinical response ($n = 17$ responders versus $n = 26$ non-responders) in samples collected at therapy baseline. **c**, Kaplan–Meier plot for PFS according to the baseline IL-17A concentration. **d**, Mono anti-PD-1-treated melanoma validation cohort (anti-PD-1 therapy, $n = 44$). **e**, Serum IL-17A levels as measured by ELISA in correlation to the best clinical response ($n = 21$ responders versus $n = 23$ non-responders) in samples collected at therapy baseline.

f, Kaplan–Meier plot for PFS according to the baseline IL-17A concentration. P values are from the unpaired t -test, and mean \pm 95% CIs are plotted in **b,e**. Each dot represents a biologically independent sample. Categorization into ‘high’ versus ‘low’ according to the X-tile-determined cut-point value was carried out separately within each dataset. HRs and 95% CIs are reported for ‘IL-17A high’, and P values are from the log-rank test in **c,f**. All P values are two tailed. Responder, complete and partial response; non-responder, progressive disease, stable disease, mixed response.

Finally, we validated these findings using a multi-center validation cohort. Baseline serum samples of 45 patients with melanoma treated with dual ICI (anti-CTLA-4 plus anti-PD-1 antibodies) and 44 patients with melanoma treated with anti-PD-1 monotherapy were independently collected across four different dermatology departments (Tübingen, Mannheim and Essen in Germany; St. Gallen in Switzerland; Fig. 6a,d). We confirmed that high baseline IL-17A levels were associated with dual-ICI response ($P = 0.0401$ responders versus non-responders; Fig. 6b) and longer PFS ($P = 0.0230$; HR, 0.36; Fig. 6c). By contrast, baseline IL-17A levels did not correlate with mono anti-PD-1 response ($P > 0.05$; Fig. 6e,f).

In conclusion, our data suggest that plasma IL-17 and T_H17 cytokines may be a valuable baseline biomarker for response prediction and patient stratification in melanoma, specifically to predict a potential benefit of adding anti-CTLA-4 to anti-PD-1 antibodies upfront to therapy. For a deeper understanding of the dynamics of immune cytokine levels under ICI, for example, to switch treatment when resistance development is imminent, extended studies with systematic longitudinal sampling protocols are needed.

Discussion

Following recent observations from clinical trials indicating that patients with *BRAF*-mutant melanoma in particular benefit from dual ICI^{1–3}, we wondered whether we could derive a molecular rationale that prospectively leads to a more general biomarker concept for ICI therapy stratification. As a starting point, we analyzed transcriptional differences between *BRAF*-mutant versus *BRAF*-WT tumors in a NanoString discovery cohort specifically focusing on known immune and resistance signatures. We found IL-17 and related T_H17 GES to be significantly enriched in *BRAF*-mutant tumors but also considered that signaling of the MAPK–extracellular signal-regulated kinase (ERK) pathway can be activated by various genetic alterations²⁹. Indeed, we found that the IL-17 GES also correlates with the presence of other oncogenic mutations in MAPK genes including *NRAS*, *KRAS* and *NFI*. However, we still found several tumor samples with high IL-17 GES, in which we could not detect common MAPK driver mutations by expanded targeted next-generation sequencing genotyping. We assumed that, in such ‘*BRAF*-, *NRAS*- and *NFI*-WT’ samples, the IL-17 pathway might be triggered by alternative regulatory factors such as RORc, STAT3

and NF- κ B³⁰, possibly resulting from unknown genetic or non-genetic activation. As activation of the MAPK pathway is prevalent in many human cancers³¹, our results may point toward a universal biomarker opportunity for IL-17, not only across different MAPK genotypes, but also across different cancer entities.

We also found patients with melanoma in our tissue and plasma cohorts who did not respond to dual ICI despite a positive *BRAF*-mutant status. Accordingly, the murine YUMML7 melanoma model (*BRAF*^{V600E}, *Pten*^{del}, *Cdkn2a*^{del}) also lacks ICI response, which could be explained by the known immune suppressive effects of deleting *Pten* and the associated impaired interferon response and T cell exclusion³². Overall, this suggests co-regulation of the IL-17 and MAPK pathways, but the IL-17 pathway is probably not exclusively regulated by oncogenic MAPK activators, nor is the response to dual ICI exclusively related to IL-17 activation. A deeper dissection of the IL-17 regulatory landscape in our tissue discovery cohort is technically not possible because of the limited number of genes that can be detected by the predefined NanoString setup. Future (single-cell) RNA-seq profiling might help to decipher such alternative mechanisms of T_H17–IL-17 stimulation. The role of IL-17 signaling and T_H17 cells in cancer progression has been controversially discussed thus far³³. Studies that evaluated the association between IL-17 and patients' prognoses are inconsistent across cancer types including melanoma^{34–36}. T_H17 cells and IL-17 are known to have both anti-tumor and pro-tumor effects. However, the underlying mechanism of IL-17 for its anti-tumor or pro-tumor effects in melanoma is not well understood³⁷. In mouse models, a few studies supported pro-tumoral activity of IL-17, where knockdown of IL-17 receptor (IL-17R) A or IL-17RC led to decreased formation of B16 melanoma tumors^{38,39}. On the other hand, IL-17A-deficient mice have been shown to be susceptible to spontaneous melanoma development⁴⁰ or formation of lung tumors⁴¹. We found across several published ICI-treated patient cohorts (in total, $n = 79$ dual ICI, $n = 134$ mono anti-PD-1 and $n = 42$ mono anti-CTLA-4 ICI-treated patients^{16–19}) that a high baseline IL-17 GES level in melanoma tissue is significantly associated with improved therapy response in dual-ICI-treated but not in mono-ICI-treated patients.

High IL-17 signature expression in ICI-treated patient cohorts was additionally positively correlated with higher infiltration of T cells, T_H17 cells, dendritic cells and neutrophils. This suggests that the role of the pre-existent cytokine milieu and that the associated immune cell populations such as neutrophils, which are commonly considered a negative predictive marker for ICI⁴², might differ depending on the exact therapeutic ICI context. Our *in silico* results together with the results from *in vivo* manipulation of IL-17 in two syngeneic melanoma ICI models suggest that the IL-17-associated presence of neutrophils could support the anti-tumor response in patients with melanoma to dual ICI. Likewise, a recent study demonstrated that T cell-mediated tumor elimination follows the recruitment of anti-tumor neutrophils that facilitate the eradication of antigen escape variants in T cell immunotherapies. Furthermore, neutrophil activation was evident in murine but also in human melanoma tumors treated with ICI⁴³. Thus, the interplay between T cells and neutrophils might represent an attractive study target to further unravel the immune mechanisms of individual ICI functions on the cellular level in the future.

IL-17A is the hallmark cytokine of T_H17 cells and is the most potent inducer of downstream cytokines and neutrophil recruitment among IL-17 family members⁴. Therefore, we focused on IL-17A for our cytokine-based approach for outcome stratification of patients with melanoma. In brief, a high baseline IL-17A level in patient plasma samples was indicative of a higher global baseline T_H17 cytokine profile preceding clinical response to dual ICI in the metastatic setting but not anti-PD-1 monotherapy. It would have also been interesting to analyze IL-17A levels in patient plasma samples from mono anti-CTLA-4-treated patients because of clinical observations made in earlier dose-ranging studies with ipilimumab. However, analysis of a mono anti-CTLA-4-treated patient cohort was not possible due to its current

limited use as a monotherapeutic agent in metastatic disease. In the ipilimumab dose-ranging study, *BRAF*-mutant patients had longer median OS than *BRAF*-WT patients with the high (10 mg per kg) but also the standard (3 mg per kg) dose of ipilimumab (33.2 versus 8 months and 19.7 versus 2 months, respectively)⁴⁴. This could indicate that actually ipilimumab is a drug that is predominantly IL-17 responsive also when given as combination in dual ICI. Furthermore, the association between IL-17 and MAPK activation may point to further biomarker opportunities for triple-combination (MAPKi and ICI) therapies, which could be addressed in future studies.

In addition, several studies have shown that the IL-17–T_H17 pathway predicts the occurrence of irAEs after ICI therapy^{45,46}. At the same time, a positive association between irAEs and response to ICI therapy has been found^{47,48}. Recent reports now suggest that inhibition of some T_H17 cytokines, such as IL-6, reduces irAEs without reducing the efficacy of ICI⁴⁹. This differs markedly from the ICI-limiting effects of IL-17 blockade shown in our study and may indicate a more non-linear function within the group of T_H17 cytokines. In fact, T_H17 cytokines are pleiotropic and produced by different cell types such as T cells, B cells and macrophages⁵⁰. Therefore, future studies are urgently needed to decipher the multifunctional role of the T_H17 cytokine network and to understand the immune mechanisms controlling irAE and the response to ICI.

In sum, our data suggest that IL-17A may serve as a biomarker for predicting response to dual-ICI therapy. IL-17A cytokine levels can be measured by common analytical biochemistry assays (for example, enzyme-linked immunosorbent assay (ELISA)) that are easily accessible and applicable in the clinical routine across institutions. To reach the full benefit of cytokine-based therapy selection, several molecular parameters, such as the normal baseline threshold or cytokine concentration dynamics under therapy, need to be investigated in larger prospective cohorts integrating systematic longitudinal sampling protocols.

Methods

This study complies with all relevant ethical regulations and was approved by the ethics committee of the University Hospital Essen, University of Duisburg-Essen (approval no. 11-4715, 21-9985-BO) and the German animal protection law (Landesamt für Natur, Umwelt und Verbraucherschutz Nordrhein-Westfalen (LANUV NRW) reference no. 81-02.04.2018.A202).

Analysis of transcriptomic datasets

The discovery cohort consisted of pretreatment tissue samples from 77 treatment-naïve *BRAF*^{V600E/K}-mutant patients with melanoma from the COMBI-v phase 3 study and 79 treatment-naïve *BRAF*-WT patients from the Dermatology Department of the University Hospital Essen⁹. Custom-designed CodeSet (containing 780 genes involved in phenotypic resistance) and the commercially available Immune Panel from NanoString (800 genes involved in immune pathways) were used to generate expression data on the NanoString platform (NanoString Technologies). Clinical parameters of the discovery patient cohort and corresponding gene expression data processing were previously described⁹. The validation cohorts consisted of open-source bulk tumor tissue transcriptomic datasets from the TCGA-SKCM cohort (ICI- and MAPKi-naïve patients with melanoma) and ICI- (Liu et al.¹⁷, [phs000452.v3.p1](https://doi.org/10.1158/1078-0432.CCR1400000); Van Allen et al.¹⁶, [phs000452.v2.p1](https://doi.org/10.1158/1078-0432.CCR1400000); Gide et al.¹⁸, [PRJEB23709](https://doi.org/10.1158/1078-0432.CCR1400000); Riaz et al.¹⁹, [GSE91061](https://doi.org/10.1158/1078-0432.CCR1400000)) or MAPKi- (Long et al.¹³, [GSE61992](https://doi.org/10.1158/1078-0432.CCR1400000); Rizo et al.¹⁴, [GSE50509](https://doi.org/10.1158/1078-0432.CCR1400000); Kakavand et al.¹⁵, [GSE99898](https://doi.org/10.1158/1078-0432.CCR1400000)) receiving patients with melanoma. Normalized and log₂ transformed RSEM counts (RNA-seq by expectation maximization) from the TCGA-SKCM cohort were retrieved from the GDAC Firehose (<http://gdac.broadinstitute.org>). In the SKCM cohort, samples with available mRNA expression and mutation data ($n = 363$) were analyzed. Normalized gene level expression in transcripts per million from the

Liu et al.¹⁷ RNA-seq dataset was downloaded as described in the original study. Raw gene expression counts from the Van Allen et al.¹⁶ study were normalized using the DESeq2 version 3.17. RNA-seq raw reads from the Gide et al.¹⁸ and Riaz et al.¹⁹ studies were downloaded and converted to transcripts per million using the kallisto method. For Kaplan–Meier curves, similar treatment arms from ICI datasets were pooled and analyzed for PFS: Liu et al. dataset, $n = 47$ for anti-CTLA-4 (pretreatment) and anti-PD-1, $n = 74$ for anti-PD-1; Gide et al. dataset, $n = 32$ for anti-CTLA-4 and anti-PD-1, $n = 41$ anti-PD-1 and for OS; Liu et al. dataset, $n = 47$ for anti-CTLA-4 (pretreatment) and anti-PD-1, $n = 74$ for anti-PD-1; Riaz et al. dataset, $n = 20$ for anti-PD-1; Gide et al. dataset, $n = 32$ for anti-CTLA-4 and anti-PD-1, $n = 40$ for anti-PD-1; Van Allen et al. dataset, $n = 42$ for anti-CTLA-4 antibodies. Categorization into low versus high IL-17A–IL-17F GES was carried out separately in each dataset according to the optimal cut point determined in X-tile²⁸. Raw gene expression profiling data from the MAPKi datasets featuring a uniform, treatment-naive *BRAF*^{V600}-mutant-positive patient cohort by Long et al., Rizos et al. and Kakavand et al. were downloaded from the Gene Expression Omnibus. Count matrices were imported into Partek Flow, where background correction, quantile normalization and log₂ transformation were carried out. In all validation datasets, the IL-17A–IL-17F GES gene family signature consisted of IL-17 family genes with reliable read counts (expression value > 0 in at least 60% of tumor samples). Gene expression values were summarized into a single GES score without weighing in the normalized dataset. Gene signatures are provided in Supplementary Table 5. Immune cell fraction enrichment analyses from RNA-seq datasets were computed according to the Bindea et al.⁵¹ immune cell signature using the xCell⁵² algorithm.

Statistics and reproducibility

The melanoma patient cohort size calculation for cytokine analyses was based on power analysis using the χ^2 statistic, assuming a relative risk of 2.0 between outcome-positive and outcome-negative proportions (type I and II errors at 0.05 and 0.20, respectively). For in vivo experiments, group size was determined based on data from preliminary experiments to detect >20% effect between groups (type I and II errors at 0.05 and 0.20, respectively). In all experiments, a minimum of $n = 4$ mice were used to ensure a balance between statistical needs and animal welfare. For all other experiments, no sample size calculation was performed; however, reproducibility of the method has been demonstrated on a minimum of three biologically independent samples. No patients or cohorts were excluded from the analyses. From public datasets, only the samples with available baseline gene expression, mutational data and clinical annotation were analyzed. Data collection and analysis were performed blinded for human cytokine analyses. Data were not randomized. Normality distribution was assessed by the D'Agostino and Pearson test. Differentially expressed gene set analyses were performed using false discovery rate (FDR) applying a two-stage step-up multiple-test correction with a cutoff of $q \leq 0.05$ (significant genes are given in Supplementary Table 1). Gene ontology and pathway enrichment analysis was performed on differentially expressed genes using the FDR ($q \leq 0.05$) approach. Statistical significance was calculated using either the unpaired *t*-test or the Mann–Whitney *U*-test (depending on normality distribution) in two-group comparisons and one-way or two-way ANOVA with multiple-comparison adjustment for more than two groups. Welch's correction was applied under the unequal standard deviation assumption. Categorical data were analyzed by Fisher's exact test or the χ^2 test. Kaplan–Meier plots were computed using survival data categorized according to the biomarker threshold determined using X-tile²⁸, and curves were compared using the log-rank test. Gene set enrichment analysis was performed using WebGestalt (version 2019)⁵³ using KEGG, functional database, with a significance cutoff of FDR ≤ 0.05 . All reported *P* values were two tailed, and $P \leq 0.05$ was considered significant. Effect size was estimated according to Hedge's *g*. Network prediction and pathway enrichment

of differentially expressed proteins were carried out with the STRING database⁵⁴. For statistical and bioinformatic data processing, GraphPad Prism (version 9.5.1), Rstudio (R-3.6.1 release) and Partek Flow (version 10.0) software was used.

Cell culture

Human melanoma cell lines with the *BRAF*^{V600} mutation (WM983B, 451Lu, WM9) were maintained at 37 °C in a humidified atmosphere with 5% CO₂. Cell lines were obtained from the Wistar Institute and cultured in 2% FBS-substituted melanoma medium ('Tu2%' medium)⁵⁵. A total of 1×10^5 cells were plated in 6-cm dishes and treated with dabrafenib–trametinib (1 nM, 0.2 nM; Selleckchem) or DMSO (0.1%; AppliChem) for 7 d. Medium containing drugs was replaced after 3 d.

The CM and LN (primary CM and lymph node metastasis: LN, derived from the *ret*-transgenic melanoma model²⁰) murine cell lines were cultured in RPMI medium supplemented with 10% FBS. YUMML7 (ATCC, CRL-3362) and YUMMER1.7 (Merck, SCC243)^{21,56} cells were cultured in DMEM/F-12 medium supplemented with 10% FBS and 1% NEAA. A total of 1×10^5 cells were plated in 6-cm dishes and treated with 25 ng ml⁻¹ rm-IL-17A or solvent (water) for 48 h. Conditioned medium was collected and centrifuged, and supernatants were used for short-term culturing of naive BM neutrophils and for cytokine assays.

Real-time quantitative PCR

Total RNA was isolated from cell pellets using the RNeasy Mini Kit according to the manufacturer's protocol (Qiagen). qPCR was carried out on the StepOnePlus (Thermo Fisher Scientific) system. Each reaction was set up in technical replicates with wells containing 10 ng total RNA, 10 μ M primer pairs, 1 \times Luna Universal One-Step Reaction Mix and 1 \times Luna WarmStart RT Enzyme Mix (Luna Universal One-Step RT–qPCR Kit, New England Biolabs). Results were analyzed with StepOne software version 2.3 (Thermo Fisher Scientific). mRNA expression was calculated using the 2^{- $\Delta\Delta$ Ct} method⁵⁷ and normalized to the geometric mean of housekeeping genes *RNA18S*, *POLR2A* or *GAPDH*. Each experiment was repeated at least twice. Primer sequences are listed in Supplementary Table 2.

In vivo studies

For all in vivo studies, 8–10-week-old female C57BL/6N or C57BL/6J mice were used. To study tumor growth kinetics under ICI and combination treatments, 5×10^5 CM cells (derived from the spontaneous MT/*ret* mouse model, *BRAF*-WT, ICI sensitive)^{20,58}, 1.5×10^6 YUMMER1.7 (*BRAF*-mutant, ICI-sensitive)²¹ or 1×10^5 YUMML7 (*BRAF*-mutant, ICI-resistant)⁵⁶ mouse melanoma cells were injected subcutaneously in PBS (YUMML7, YUMMER1.7) or in a 1:1 mixture of PBS with Matrigel (CM). The following treatments in different combinations (total injection volume of 200 μ l) were administered by intraperitoneal injection: control IgG (IgG2a isotype control clone 2A3, BioXCell, 10 mg per kg body weight, 3 \times per week) anti-CTLA-4 antibody (anti-mouse CTLA-4 clone 9D9, BioXCell, 8 mg per kg body weight, 3 \times per week), anti-PD-1 antibody (anti-mouse PD1 clone RMP1-14, BioXCell, 10 mg per kg body weight, 3 \times per week), rm-IL-17A (IL-17A mouse recombinant, Prospec, 0.01 mg per kg body weight, daily), α -IL-17A (Ultra-LEAF purified anti-mouse IL-17A antibody clone TC11-18H10.1, BioLegend, 4 mg per kg body weight, 3 \times per week), anti-Ly6G antibody (anti-mouse Ly6G clone 1A8, Leinco Technologies, 4 mg per kg body weight, 3 \times per week, starting from day -2) according to the treatment schedule summarized in the schematics above the corresponding growth curves. Pretreatment with ICI was carried out for the CM model⁵⁸. Mice were randomized to different combinatorial treatment groups when tumors became palpable. Treatment continued until tumors had reached the maximal volume (not exceeding 1,500 mm³) or became ulcerated. Tumor growth kinetics were analyzed in long-term experiments, while short-term experiments (end of treatment on day 9 or day 12) were set up to analyze immune infiltration by multiplex immunofluorescence

or flow cytometry and serum cytokine profiles by multiplex cytokine array. Tumor volume was assessed by caliper measurement (calculated as $W \times W \times L \div 2$). At the end of the treatment, animals were killed, and tumor and blood samples were collected. Tumor samples were fixed in formalin for histological assessment and immunostaining. Blood samples were collected by cardiac puncture in Microvette 100 Serum tubes (Sarstedt). Serum was separated by a standard centrifugation protocol and stored at -80°C until analysis. Serum samples with substantial hemolysis from red blood cells were excluded from cytokine analyses. TANs were isolated by flow cytometry (CD45⁺CD11b⁺Ly6G⁺ sorted fraction) from single-cell suspensions derived from tumors 8 d (mean tumor volume, $\sim 250\text{ mm}^3$) after subcutaneous injection with CM or LN cells (5×10^5) in 8–10-week-old C57BL/6N mice. For proteomic analysis, proteins were liberated by cell lysis. After sample purification and tryptic digestion, peptides were analyzed by LC-MS/MS. All animal experiments were performed in accordance with institutional and national guidelines and regulations. Ethical approval was provided by the local state authority LANUV NRW in compliance with the German animal protection law (reference number 81-02.04.2018.A202).

Immune cell isolation and in vitro analysis

Naive BM neutrophils were isolated from femurs of 10-week-old female C57BL/6N mice with the mouse Neutrophil Isolation Kit (Miltenyi) using anti-biotin microbead technology according to the instruction manual by the manufacturer. Purity was confirmed by flow cytometry and the $>90\%$ CD45⁺CD11b⁺Ly6G⁺ fraction was accepted for downstream analysis. Isolated neutrophils were cultured short-term (24 h) in either RPMI with 10% FBS or conditioned medium derived from untreated or rm-IL-17A (25 ng ml⁻¹ mouse recombinant IL-17 Prospec)-treated CM mouse melanoma cells. In some experiments, α -IL-17A (5 $\mu\text{g ml}^{-1}$ Ultra-LEAF purified anti-mouse IL-17A antibody clone TC11-18H10.1, BioLegend) was added to the culture medium. Cell culture supernatants were centrifuged and used for cytokine analysis. Cell pellets were used for RNA isolation and downstream qPCR analysis. Primer sequences are provided in Supplementary Table 2.

CD8⁺ T cells were isolated from spleen tissues of 10-week-old female C57BL/6N mice using the mouse CD8a⁺ T Cell Isolation Kit (Miltenyi) according to the instruction manual by the manufacturer. Purity was confirmed by flow cytometry, and the $>90\%$ CD45⁺CD3⁺CD8⁺ fraction was accepted for downstream analysis. A total of 1.5×10^5 CD8⁺ T cells were plated in migration medium (RPMI with 1% BSA) in the upper chamber of a Boyden chamber (6.5-mm Transwell with 5.0 μm Pore Polycarbonate Membrane Insert, Corning), and 600 μl conditioned media from different treatments were added to the bottom chamber. The different conditioned media were from untreated or rm-IL-17A (25 ng ml⁻¹ mouse recombinant IL-17 Prospec)-treated CM melanoma cells with or without the downstream culturing step with BM neutrophils. In some experiments, α -IL-17A (5 $\mu\text{g ml}^{-1}$ Ultra-LEAF purified anti-mouse IL-17A antibody clone TC11-18H10.1, BioLegend) was added to the upper chamber for the duration of the migration. Serum-free medium was used as the negative control, and 200 ng ml⁻¹ mouse recombinant CXCL10 diluted in PBS with 1% BSA was used as the positive control. After 12–18 h of migration at 37 $^{\circ}\text{C}$ in a humidified atmosphere with 5% CO₂, living (Trypan blue-negative) migrated cells were counted under the microscope using a Neubauer chamber.

Multiplex immunofluorescence

Multiplex immunofluorescence staining of 4- μm , formalin-fixed paraffin-embedded mouse tumor tissue sections (three mice for each combination drug treatment group) was executed. Deparaffinization and antigen retrieval was performed using the Dako PT Link heat-induced antigen retrieval solution with high-pH (pH 9) target retrieval solution (Dako). Next, each tissue slide was stained in three consecutive rounds of antibody staining, using the Opal Multiplex IHC Kit (Akoya).

The slides were washed with Tris-buffered saline containing 0.05% Tween-20, and the microwave treatment was performed in Tris-EDTA buffer (pH 9). If the antibody host species were neither rabbit nor mouse (as provided in the kit), a horseradish peroxidase-conjugated secondary antibody for mouse or hamster (Jackson ImmunoResearch) was used at 1:1,000 in antibody diluent (Akoya Biosciences), followed by TSA visualization with Opal fluorophores (Akoya Biosciences) diluted in 1 \times Plus Amplification Diluent (Akoya Biosciences). The immunofluorescence panels consisted of melan A (EPR20380, 1:1,000, Abcam), Ly6G (RB6-8C5, 1:100, BioLegend), CD8a (C8/144B, 1:100, BioLegend), CD11c (N418, 1:100, BioLegend), CD4 (RM4-5, 1:100, BioLegend) and IL-17A (TC11-18H10.1, 1:100, BioLegend) primary antibodies. Nuclei were stained with DAPI. Imaging was performed with Zeiss Axio Scan ($\times 20$ objective) microscopy. The relative contribution of immune cells was calculated by quantitating the background-corrected mean fluorescence intensity of each marker at five random fields per tumor tissue and normalized to DAPI values. Quantitation was performed with ImageJ Fiji software following guidelines by Shihaan et al.⁵⁹

Flow cytometry analysis

Tissues were digested using the Mouse Tumor Dissociation Kit (Miltenyi) on the gentleMACS device (Miltenyi) according to the manufacturer's instructions. Red blood cell lysis buffer (BioLegend) was used to remove red blood cells. After washing with PBS, cells were incubated with TruStain fcX anti-mouse CD16/32 receptor blocking agent (BioLegend) diluted in Cell Staining Buffer (BioLegend) for 20 min at 4 $^{\circ}\text{C}$. After washing, Zombie NIR cell viability dye (1:2,000, BioLegend) was added and incubated for 20 min at 4 $^{\circ}\text{C}$. To assess immune cell composition, the following antibodies were added for 30 min at 4 $^{\circ}\text{C}$: for lymphocytes, anti-CD45 PerCP Cy5.5 (30-F11, 1:100), anti-CD3 FITC (17A2, 1:100), anti-CD4 PB (RM4-5, 1:100), anti-CD8a BV 510 (53-6.7, 1:100) and anti-granzyme B AF 647 (GB11, 1:100); for macrophages, anti-CD45 PerCP Cy5.5 (30-F11, 1:100), anti-CD11b PB (MI/70, 1:100), anti-CD11c AF 488 (N418, 1:100), anti-Ly6c AF 647 (HK1.4, 1:100) and anti-Ly6G PE (1A8, 1:100), all from BioLegend. Granzyme B was added after surface staining was completed and after fixation–permeabilization (Fixation Buffer, BioLegend; 10 \times Intracellular Staining Perm Wash Buffer, BioLegend). Subsequently, samples were washed twice before data acquisition on the BD Aria III flow cytometer. The gating strategy is shown in Extended Data Fig. 3b.

Human patient-derived tumor fragments

PDFT cultures were performed as previously described²². In short, tumor specimens were collected from three patients with melanoma undergoing surgery. The tissue was manually dissected into fragments of 1–2 mm³ and cryopreserved in freezing medium (FCS supplemented with 10% DMSO) until use. Tumor fragments were thawed and embedded in artificial matrix (Cultrex UltiMatrix (Bio-Techne, 2 mg ml), rat tail collagen I (Corning, 1 mg ml⁻¹), sodium bicarbonate (Sigma-Aldrich, 1.1%) and DMEM tumor medium (Thermo Fisher Scientific) supplemented with 1 mM sodium pyruvate (Sigma-Aldrich), 1 \times MEM nonessential amino acids (Sigma-Aldrich), 2 mM L-glutamine (Thermo Fisher Scientific), 10% FBS and 1% penicillin-streptomycin) in a 96-well plate, using 8–10 fragments for each treatment condition. For PDFT stimulation, the medium was supplemented with anti-PD-1 (10 $\mu\text{g ml}^{-1}$, nivolumab, Bristol Myers Squibb), anti-CTLA-4 (10 $\mu\text{g ml}^{-1}$, ipilimumab, Bristol Myers Squibb) and α -IL-17A (10 $\mu\text{g ml}^{-1}$, clone BL168, BioLegend) antibodies. After 48 h of incubation at 37 $^{\circ}\text{C}$, supernatants were collected, and chemokine and cytokine secretion was assessed using the LEGENDplex Human Th Cytokine and Human Proinflammatory Chemokine assays, according to the manufacturer's protocol.

Patient samples

Plasma samples ($n = 117$) from 70 patients with melanoma who received first-line ipilimumab plus nivolumab and plasma samples ($n = 76$)

from 51 patients with melanoma who received first-line nivolumab or pembrolizumab were collected at therapy baseline and before the first staging evaluation (median, week 9; range, 2–12 weeks). All patients were treated at the Department of Dermatology of the University Hospital Essen in standard-of-care or clinical trial settings. Serum samples ($n = 89$) from patients with melanoma who received ipilimumab plus nivolumab ($n = 45$) or nivolumab or pembrolizumab ($n = 44$) were collected at therapy baseline across four independent centers (Tübingen, Mannheim and Essen in Germany; St. Gallen in Switzerland). Baseline clinicopathological characteristics are given in Supplementary Tables 3 and 4. Radiologic tumor response was evaluated by an independent radiologist according to RECIST criteria. Patients with complete response and partial response were classified as responders, while those with mixed response and progressive disease were classified as non-responders. For the Essen cohorts, human biological samples and related data were provided by the Westdeutsche Biobank Essen (WBE/SCABIO, University Hospital Essen, University of Duisburg-Essen, Essen, Germany; approval nos. II-4715, 21-9985-BO). The samples were prospectively collected and archived at the local WBE/SCABIO biobank according to institutional informed consent procedures and retrospectively evaluated for this study. Serum samples in the validation cohorts were collected in compliance with the ethical regulations of the respective institutions, and approval was provided by the ethical committee of Tübingen University Medical Center (490/2014 B01, 089/2021A), the Ethical Committee II of Heidelberg University (2010-318N-MA) and Ethikkommission Ostschweiz (EKOS 16/079). Resected tumor samples were collected from patients with melanoma undergoing surgical treatment at the Netherlands Cancer Institute (NKI-AVL), the Netherlands. The study was approved by the institutional review board of the NKI-AVL (CFMPB484) and executed in compliance with ethical regulations. All patients consented to the research usage of material not required for diagnostics via prior informed consent.

Secreted cytokine profiling

Secreted levels of human or mouse IL-17A in plasma or serum were determined according to the manufacturer's instructions (LEGEND MAX Human IL-17A ELISA Kit, LEGEND MAX Mouse IL-17A ELISA Kit, BioLegend). For human samples, plasma samples from patients with psoriasis were used as internal reference controls. For multiplex quantification of cytokines, the bead-based LEGENDplex panels (Human Th17 7-plex Panel; Human Th12-plex Panel, Mouse Th17 7-plex Panel; IL-1 β , IL-23 and IL-12p70 from the Inflammation Panel I; granzyme A and granzyme B from the CD8/NK Panel, predefined and custom-designed mix-and-match system from BioLegend) were used according to the manufacturer's instructions. Flow cytometry reading was performed on the FACSAria III (BD). Mean fluorescence intensity values were recorded using LEGENDplex analysis software (version 2021.07.01), and cytokine concentrations (pg ml⁻¹) were interpolated from a five-parameter logistic non-linear curve model using a separate standard curve for each cytokine. For prognostic stratification of IL-17A plasma levels, an optimal cut point was determined in each dataset separately using X-tile²⁸.

Reporting summary

Further information on research design is available in the Nature Portfolio Reporting Summary linked to this article.

Data availability

Previously published RNA-seq data that were reanalyzed here are available under accession codes [phs000452.v3.p1](#) (Liu et al.¹⁷), [phs000452.v2.p1](#) (Van Allen et al.¹⁶), [PRJEB23709](#) (Gide et al.¹⁸), [GSE91061](#) (Riaz et al.¹⁹), [GSE61992](#) (Long et al.¹³), [GSE50509](#) (Rizos et al.¹⁴) and [GSE99898](#) (Kakavand et al.¹⁵). Data from the discovery cohort (Brase et al.⁹) that were derived from the COMBI-v trial (Novartis) were obtained directly from the authors with the permission of Novartis. Novartis

is committed to sharing with qualified external researchers access to patient-level data and supporting clinical documents from eligible studies. Requests are reviewed and approved by an independent review panel on the basis of scientific merit. All data provided are anonymized to respect the privacy of patients who have participated in the trial in line with applicable laws and regulations. This trial data availability is according to the criteria and process described at <https://clinicalstudydatarequest.com>. Human melanoma RNA-seq data were derived from the TCGA Research Network: <http://cancergenome.nih.gov/>. All other data supporting the findings of this study are available from the corresponding author on reasonable request. Source data are provided with this paper.

Code availability

Only open-source software was used for this study, and no custom codes were generated for RNA-seq analysis.

References

1. Wolchok, J. D. et al. Long-term outcomes with nivolumab plus ipilimumab or nivolumab alone versus ipilimumab in patients with advanced melanoma. *J. Clin. Oncol.* **40**, 127–137 (2022).
2. Larkin, J. et al. Five-year survival with combined nivolumab and ipilimumab in advanced melanoma. *N. Engl. J. Med.* **381**, 1535–1546 (2019).
3. Zimmer, L. et al. Adjuvant nivolumab plus ipilimumab or nivolumab monotherapy versus placebo in patients with resected stage IV melanoma with no evidence of disease (IMMUNED): a randomised, double-blind, placebo-controlled, phase 2 trial. *Lancet* **400**, 1117–1129 (2020).
4. Iwakura, Y., Ishigame, H., Saijo, S. & Nakae, S. Functional specialization of interleukin-17 family members. *Immunity* **34**, 149–162 (2011).
5. Yao, Z. et al. Human IL-17: a novel cytokine derived from T cells. *J. Immunol.* **155**, 5483–5486 (1995).
6. Mills, K. H. G. IL-17 and IL-17-producing cells in protection versus pathology. *Nat. Rev. Immunol.* **23**, 38–54 (2023).
7. Miossec, P. & Kolls, J. K. Targeting IL-17 and T_H17 cells in chronic inflammation. *Nat. Rev. Drug Discov.* **11**, 763–776 (2012).
8. Vajaitu, C. et al. The central role of inflammation associated with checkpoint inhibitor treatments. *J. Immunol. Res.* **2018**, 4625472 (2018).
9. Brase, J. C. et al. Role of tumor-infiltrating B cells in clinical outcome of patients with melanoma treated with dabrafenib plus trametinib. *Clin. Cancer Res.* **27**, 4500–4510 (2021).
10. Noubade, R. et al. Activation of p38 MAPK in CD4 T cells controls IL-17 production and autoimmune encephalomyelitis. *Blood* **118**, 3290–3300 (2011).
11. Martel-Pelletier, J., Mineau, F., Jovanovic, D., Di Battista, J. A. & Pelletier, J. P. Mitogen-activated protein kinase and nuclear factor κ B together regulate interleukin-17-induced nitric oxide production in human osteoarthritic chondrocytes: possible role of transactivating factor mitogen-activated protein kinase-activated protein kinase. *Arthritis Rheum.* **42**, 2399–2409 (2001).
12. Schubert, M. et al. Perturbation-response genes reveal signaling footprints in cancer gene expression. *Nat. Commun.* **9**, 20 (2018).
13. Long, G. V. et al. Increased MAPK reactivation in early resistance to dabrafenib/trametinib combination therapy of BRAF-mutant metastatic melanoma. *Nat. Commun.* **5**, 5694 (2014).
14. Rizos, H. et al. BRAF inhibitor resistance mechanisms in metastatic melanoma: spectrum and clinical impact. *Clin. Cancer Res.* **20**, 1965–1977 (2014).
15. Kakavand, H. et al. PD-L1 expression and immune escape in melanoma resistance to MAPK inhibitors. *Clin. Cancer Res.* **23**, 6054–6061 (2017).

16. Van Allen, E. M. et al. Genomic correlates of response to CTLA-4 blockade in metastatic melanoma. *Science* **350**, 207–211 (2015).
17. Liu, D. et al. Integrative molecular and clinical modeling of clinical outcomes to PD1 blockade in patients with metastatic melanoma. *Nat. Med.* **25**, 1916–1927 (2019).
18. Gide, T. N. et al. Distinct immune cell populations define response to anti-PD-1 monotherapy and anti-PD-1/anti-CTLA-4 combined therapy. *Cancer Cell* **35**, 238–255 (2019).
19. Riaz, N. et al. Tumor and microenvironment evolution during immunotherapy with nivolumab. *Cell* **171**, 934–949 (2017).
20. Helfrich, I., Ullrich, N., Zigrino, P. & Schadendorf, D. Primary tumor versus metastasis: new experimental models for studies on cancer cell homing and metastasis in melanoma. *Pigment Cell Melanoma Res.* **27**, 309–316 (2014).
21. Wang, J. et al. UV-induced somatic mutations elicit a functional T cell response in the YUMMER1.7 mouse melanoma model. *Pigment Cell Melanoma Res.* **30**, 428–435 (2017).
22. Voabil, P. et al. An ex vivo tumor fragment platform to dissect response to PD-1 blockade in cancer. *Nat. Med.* **27**, 1250–1261 (2021).
23. Kaptein, P. et al. Addition of interleukin-2 overcomes resistance to neoadjuvant CTLA4 and PD1 blockade in ex vivo patient tumors. *Sci. Transl. Med.* **14**, eabj9779 (2022).
24. Grasso, C. S. et al. Conserved interferon- γ signaling drives clinical response to immune checkpoint blockade therapy in melanoma. *Cancer Cell* **38**, 500–515 (2020).
25. Tumeh, P. C. et al. PD-1 blockade induces responses by inhibiting adaptive immune resistance. *Nature* **515**, 568–571 (2014).
26. Hoch, T. et al. Multiplexed imaging mass cytometry of the chemokine milieu in melanoma characterizes features of the response to immunotherapy. *Sci. Immunol.* **7**, eabk1692 (2022).
27. Daley, J. M., Thomay, A. A., Connolly, M. D., Reichner, J. S. & Albina, J. E. Use of Ly6G-specific monoclonal antibody to deplete neutrophils in mice. *J. Leukoc. Biol.* **83**, 64–70 (2008).
28. Camp, R. L., Dolled-Filhart, M. & Rimm, D. L. X-tile: a new bioinformatics tool for biomarker assessment and outcome-based cut-point optimization. *Clin. Cancer Res.* **10**, 7252–7259 (2004).
29. Curtin, J. A. et al. Distinct sets of genetic alterations in melanoma. *N. Engl. J. Med.* **353**, 2135–2147 (2005).
30. Khan, D. & Ahmed, S. A. Regulation of IL-17 in autoimmune diseases by transcriptional factors and microRNAs. *Front. Genet.* **6**, 236 (2015).
31. Ullah, R., Yin, Q., Snell, A. H. & Wan, L. RAF–MEK–ERK pathway in cancer evolution and treatment. *Semin. Cancer Biol.* **85**, 123–154 (2022).
32. Peng, W. et al. Loss of PTEN promotes resistance to T cell-mediated immunotherapy. *Cancer Discov.* **6**, 202–216 (2016).
33. Ruiz de Morales, J. M. G. et al. Critical role of interleukin (IL)-17 in inflammatory and immune disorders: an updated review of the evidence focusing in controversies. *Autoimmun. Rev.* **19**, 102429 (2020).
34. Kuen, D. S., Kim, B. S. & Chung, Y. IL-17-producing cells in tumor immunity: friends or foes? *Immune Netw.* **20**, e6 (2020).
35. Bernardini, N. et al. IL-17 and its role in inflammatory, autoimmune, and oncological skin diseases: state of art. *Int. J. Dermatol.* **59**, 406–411 (2020).
36. Wilke, C. M. et al. T_H17 cells in cancer: help or hindrance? *Carcinogenesis* **32**, 643–649 (2011).
37. Chen, C. & Gao, F. H. T_H17 cells paradoxical roles in melanoma and potential application in immunotherapy. *Front. Immunol.* **10**, 187 (2019).
38. Chen, Y. S. et al. Locally targeting the IL-17/IL-17RA axis reduced tumor growth in a murine B16F10 melanoma model. *Hum. Gene Ther.* **30**, 273–285 (2019).
39. Yan, C. et al. IL-17RC is critically required to maintain baseline A20 production to repress JNK isoform-dependent tumor-specific proliferation. *Oncotarget* **8**, 43153–43168 (2017).
40. Martin-Orozco, N. et al. T helper 17 cells promote cytotoxic T cell activation in tumor immunity. *Immunity* **31**, 787–798 (2009).
41. Kryczek, I., Wei, S., Szeliga, W., Vatan, L. & Zou, W. Endogenous IL-17 contributes to reduced tumor growth and metastasis. *Blood* **114**, 357–359 (2009).
42. Li, M. et al. Change in neutrophil to lymphocyte ratio during immunotherapy treatment is a non-linear predictor of patient outcomes in advanced cancers. *J. Cancer Res. Clin. Oncol.* **145**, 2541–2546 (2019).
43. Hirschhorn, D. et al. T cell immunotherapies engage neutrophils to eliminate tumor antigen escape variants. *Cell* **186**, 1432–1447 (2023).
44. Ascierto, P. A. et al. Overall survival at 5 years of follow-up in a phase III trial comparing ipilimumab 10 mg/kg with 3 mg/kg in patients with advanced melanoma. *J. Immunother. Cancer* **8**, e000391 (2020).
45. Ribas, A. et al. Tremelimumab (CP-675,206), a cytotoxic T lymphocyte associated antigen 4 blocking monoclonal antibody in clinical development for patients with cancer. *Oncologist* **12**, 873–883 (2007).
46. Tarhini, A. et al. Baseline circulating IL-17 predicts toxicity while TGF- β 1 and IL-10 are prognostic of relapse in ipilimumab neoadjuvant therapy of melanoma. *J. Immunother. Cancer* **3**, 39 (2015).
47. Cortellini, A., Buti, S., Agostinelli, V. & Bersanelli, M. A systematic review on the emerging association between the occurrence of immune-related adverse events and clinical outcomes with checkpoint inhibitors in advanced cancer patients. *Semin. Oncol.* **46**, 362–371 (2019).
48. Eggermont, A. M. M. et al. Association between immune-related adverse events and recurrence-free survival among patients with stage III melanoma randomized to receive pembrolizumab or placebo: a secondary analysis of a randomized clinical trial. *JAMA Oncol.* **6**, 519–527 (2020).
49. Hailemichael, Y. et al. Interleukin-6 blockade abrogates immunotherapy toxicity and promotes tumor immunity. *Cancer Cell* **40**, 509–523 (2022).
50. Guéry, L. & Hugues, S. T_H17 cell plasticity and functions in cancer immunity. *BioMed Res. Int.* **2015**, 314620 (2015).
51. Bindea, G. et al. Spatiotemporal dynamics of intratumoral immune cells reveal the immune landscape in human cancer. *Immunity* **39**, 782–795 (2013).
52. Aran, D., Hu, Z. & Butte, A. J. xCell: digitally portraying the tissue cellular heterogeneity landscape. *Genome Biol.* **18**, 220 (2017).
53. Liao, Y., Wang, J., Jaehnig, E. J., Shi, Z. & Zhang, B. WebGestalt 2019: gene set analysis toolkit with revamped UIs and APIs. *Nucleic Acids Res.* **47**, W199–W205 (2019).
54. Szklarczyk, D. et al. The STRING database in 2023: protein–protein association networks and functional enrichment analyses for any sequenced genome of interest. *Nucleic Acids Res.* **51**, D638–D646 (2023).
55. Chauvistré, H. et al. Persister state-directed transitioning and vulnerability in melanoma. *Nat. Commun.* **13**, 3055 (2022).
56. Meeth, K., Wang, J. X., Micevic, G., Damsky, W. & Bosenberg, M. W. The YUMM lines: a series of congenic mouse melanoma cell lines with defined genetic alterations. *Pigment Cell Melanoma Res.* **29**, 590–597 (2016).
57. Schmittgen, T. D. & Livak, K. J. Analysis of relative gene expression data using real-time quantitative PCR and the $2^{-\Delta\Delta C(t)}$ method. *Methods* **25**, 402–408 (2001).

58. Michel, L. et al. Targeting early stages of cardiotoxicity from anti-PD1 immune checkpoint inhibitor therapy. *Eur. Heart J.* **43**, 316–329 (2022).
59. Shihan, M. H., Novo, S. G., Le Marchand, S. J., Wang, Y. & Duncan, M. K. A simple method for quantitating confocal fluorescent images. *Biochem. Biophys. Rep.* **25**, 100916 (2021).

Acknowledgements

We express our gratitude to A. Höwner, S. Scharfenberg, V. Schröder and P. Braß for the excellent technical assistance. We thank L.M. Nascentes Melo and G. Allies for helping with flow cytometry data analysis. We thank A. Squire and A. Brenzel from the Imaging Center Essen (IMCES) for their technical support. We thank M. Herlyn for providing the WM983B, 451Lu and WM9 cell lines. Illustrations were created with <https://biorender.com> and partly using modified pictures from Servier Medical Art, provided by Servier, licensed under a Creative Commons Attribution 3.0 unported license. This study was supported by funding from Novartis (R.V.), Brigitte und Dr. Konstanze Wegener-Stiftung (R.V.) and the German Research Foundation (DFG, Deutsche Forschungsgemeinschaft; KFO 337, SFB1430): RO 3577/7-1, 424228829 (A.R.), SCHA 422/17-1 (D.S.), HE 5294/2-1 (I.H.), PA 2376/1-1 (A.P.), HO 6389/2-1 (S.H.), RU/FOR5427 SP4, EN984/15-1, EN984/16-1, CRC/TR296 P09, CRC/TR332 A3, and CRC/TR332 Z1 (DRE).

Author contributions

Conceptualization: R.V., L.Z., I.H., D.S., A.R. Methodology: R.V., L.Z., Y.A.-M., P.K., L.J.A., B.S., J.C.B., D.G., T.A., N.W., J.U., L.F., F.R., H.C.R., J.D., D.R.E., S.H., S.U., W.S., E.L., A.S., A.P., F.Z., J.M.P., J.M.K., W.P.F., D.S.T., I.H. Investigation: R.V., L.Z., Y.A.-M., P.K., L.J.A., B.S., T.A., N.W., S.H., J.M.P. Visualization: R.V. Funding acquisition: R.V., I.H., A.P., S.H., D.R.E., D.S., A.R. Project administration: A.S., A.P., I.H., D.S., A.R. Supervision: D.S., A.R. Writing (original draft): R.V., A.R. Writing (review and editing): all authors.

Competing interests

D.S. served as a consultant and/or has received honoraria from Array, Roche, Bristol Myers Squibb, Merck Sharp & Dohme, Nektar, NeraCare, Novartis, Pierre Fabre, Philogen, Pfizer, Sandoz, Sun Pharma and Sanofi; research funding to their institution from Novartis, Amgen, Roche, MSD and Array; and travel support from Merck Sharp & Dohme, Bristol Myers Squibb, Pierre Fabre, Sun Pharma, Sanofi and Novartis, outside the submitted work. E.L. served as a consultant and/or has received honoraria from Bristol Myers Squibb, Merck Sharp & Dohme, Novartis, Pierre Fabre, Sanofi, Sun Pharma and Takeda and travel support from Bristol Myers Squibb, Pierre Fabre, Sun Pharma and Novartis, outside the submitted work. A.R. reports grants from Novartis, Bristol Myers Squibb and Adtec; personal fees from Novartis, Bristol Myers Squibb and Merck Sharp & Dohme; and nonfinancial support from Amgen, Roche, Merck Sharp & Dohme, Novartis, Bristol Myers Squibb and Teva, outside the submitted work. W.P.F. reports fees from Calyx (consultant), RadioMedix (image review), Bayer (speaker bureau) and Parexel (image review), outside the submitted work. J.M.P. served as a consultant and/or has received honoraria from Bristol Myers Squibb, Novartis and Sanofi and has received travel support from Bristol Myers Squibb, Novartis and Therakos, outside the submitted work. L.J.A. received honoraria from Novartis, Sun Pharma and Bristol Myers Squibb and travel support from Sun Pharma, Takeda and Sanofi, outside the submitted work. S.U. declares research support from Bristol Myers Squibb and Merck Serono; speaker and advisory board honoraria from Bristol Myers Squibb, Merck Sharp & Dohme, Merck Serono, Novartis and Roche and travel support from Bristol Myers Squibb, Merck Sharp & Dohme and Pierre Fabre, outside the submitted work. W.S. reports grants from medi,

grants and personal fees from Novartis and Almirall and personal fees from Amgen, AbbVie, Janssen, Boehringer Ingelheim, Bristol Myers Squibb, Lilly, UCB Novartis, Pfizer, LEO Pharma and Sanofi Genzyme, outside the submitted work. J.C.B. reports employment with Novartis and ownership of Novartis stock. D.G. reports employment with Novartis. J.U. is on the advisory board or has received honoraria and travel support from Amgen, Bristol Myers Squibb, GSK, Immunocore, Leo Pharma, Merck Sharp & Dohme, Novartis, Pierre Fabre, Roche and Sanofi, outside the submitted work. L.Z. declares speaker and advisory board honoraria from Bristol Myers Squibb, Merck Sharp & Dohme, Novartis, Pierre Fabre, Sanofi, Sun Pharma, research support from Novartis and travel support from Merck Sharp & Dohme, Bristol Myers Squibb, Pierre Fabre, Sanofi, Sun Pharma and Novartis, outside the submitted work. H.C.R. received consulting and lecture fees from AbbVie, AstraZeneca, Roche, Bristol Myers Squibb, Vertex, SinABiomedics and Merck. H.C.R. received research funding from AstraZeneca and Gilead Pharmaceuticals. H.C.R. is a cofounder of CDL Therapeutics. D.S.T. reports grants from Bristol Myers Squibb and Asher Biotherapeutics and speaker honoraria from Boehringer Ingelheim and served as a consultant for Ysios Capital and iTEOS, outside the submitted work. T.A. reports personal fees from CeCaVa, institutional grants and personal fees from Novartis, institutional grants from NeraCare, personal fees and travel grants from BMS, personal fees from Pierre Fabre, institutional grants from Sanofi, institutional grants from SkylineDx and institutional grants from iFIT, outside the submitted work. All other authors declare no competing interest.

Additional information

Extended data is available for this paper at

<https://doi.org/10.1038/s43018-023-00610-2>.

Supplementary information The online version contains supplementary material available at <https://doi.org/10.1038/s43018-023-00610-2>.

Correspondence and requests for materials should be addressed to Alexander Roesch.

Peer review information *Nature Cancer* thanks Adil Daud, Jason Luke and the other, anonymous, reviewer(s) for their contribution to the peer review of this work.

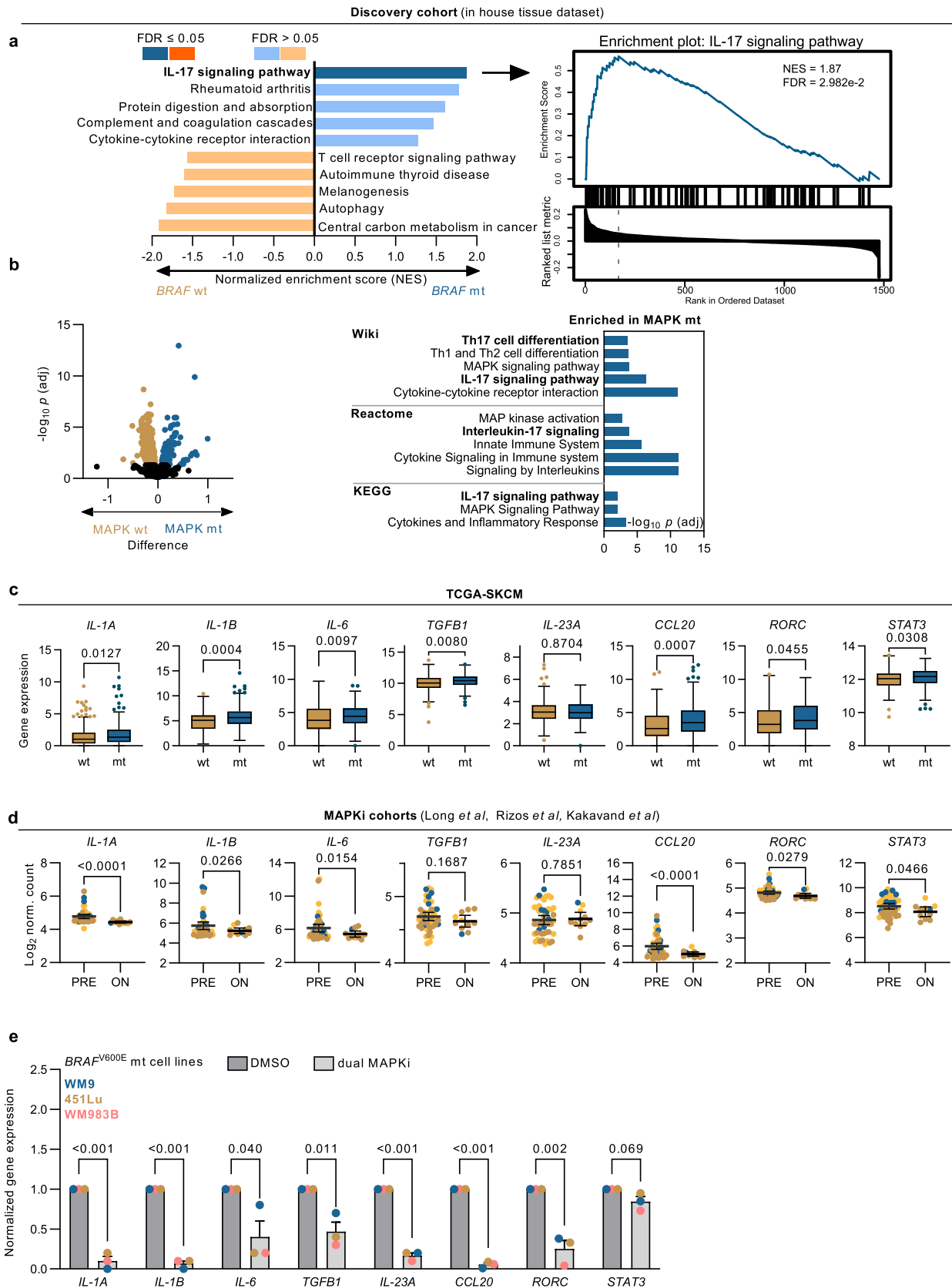
Reprints and permissions information is available at www.nature.com/reprints.

Publisher's note Springer Nature remains neutral with regard to jurisdictional claims in published maps and institutional affiliations.

Open Access This article is licensed under a Creative Commons Attribution 4.0 International License, which permits use, sharing, adaptation, distribution and reproduction in any medium or format, as long as you give appropriate credit to the original author(s) and the source, provide a link to the Creative Commons license, and indicate if changes were made. The images or other third party material in this article are included in the article's Creative Commons license, unless indicated otherwise in a credit line to the material. If material is not included in the article's Creative Commons license and your intended use is not permitted by statutory regulation or exceeds the permitted use, you will need to obtain permission directly from the copyright holder. To view a copy of this license, visit <http://creativecommons.org/licenses/by/4.0/>.

© The Author(s) 2023, corrected publication 2023

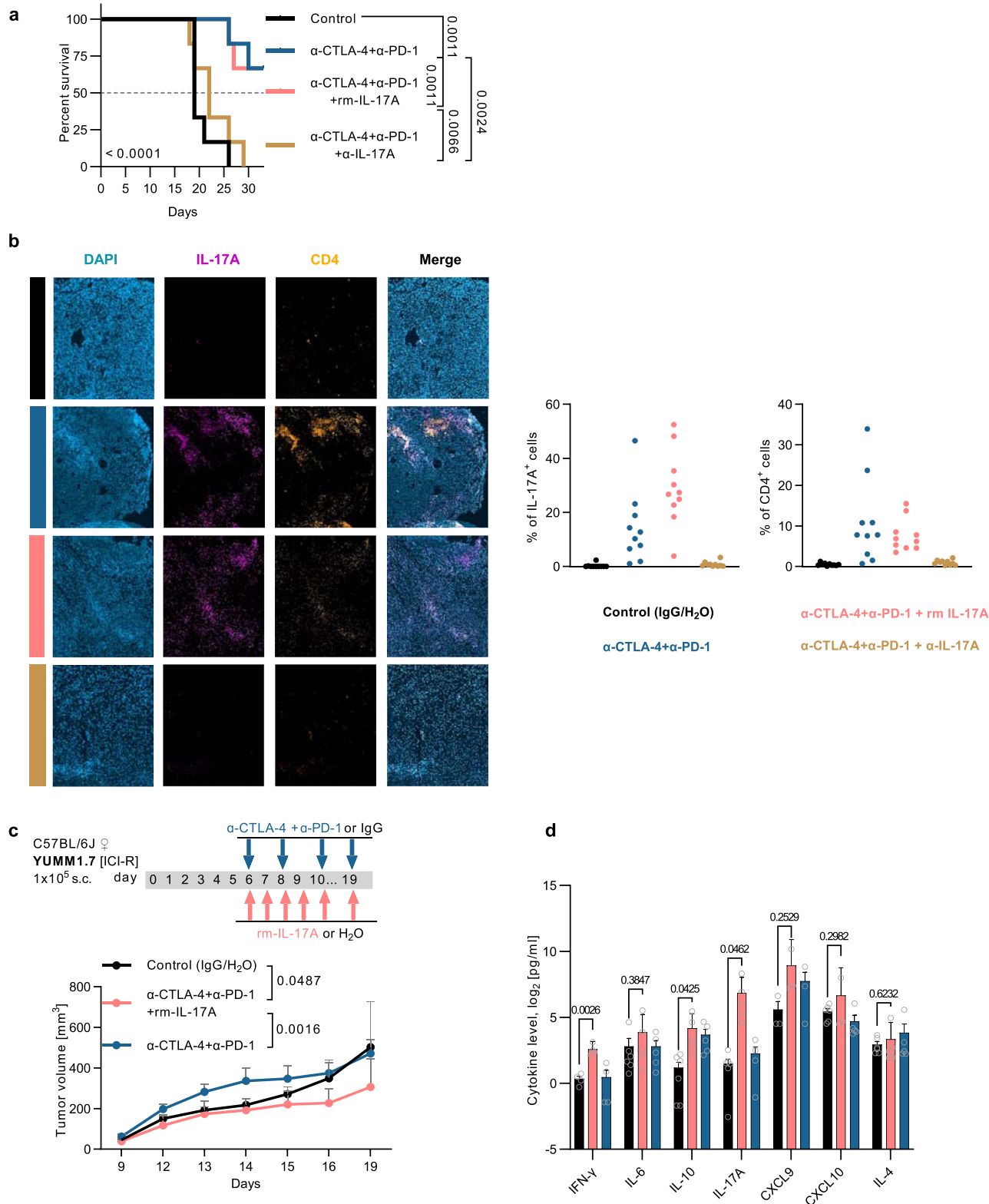
¹Department of Dermatology, University Hospital Essen, West German Cancer Center, University Duisburg-Essen and the German Cancer Consortium (DKTK), Essen, Germany. ²Division of Molecular Oncology and Immunology, the Netherlands Cancer Institute, Amsterdam, the Netherlands. ³Novartis Pharma AG, Basel, Switzerland. ⁴Novartis Institutes for BioMedical Research, Inc., Cambridge, MA, USA. ⁵Department of Dermatology, University Hospital of Tübingen, Tübingen, Germany. ⁶Institute of Immunobiology, Kantonsspital St. Gallen, Switzerland, Switzerland. ⁷Skin Cancer Unit, German Cancer Research Center (DKFZ), Heidelberg, Germany. ⁸Department of Dermatology, Venereology and Allergology, University Medical Center Mannheim, Ruprecht Karls University of Heidelberg, Mannheim, Germany. ⁹DKFZ Hector Cancer Institute at the University Medical Center Mannheim, Mannheim, Germany. ¹⁰Department of Applied Computational Cancer Research, Institute for AI in Medicine (IKIM), University Hospital Essen, Essen, Germany. ¹¹Department of Hematology and Stem Cell Transplantation, University Hospital Essen, Essen, Germany. ¹²Center for Medical Biotechnology (ZMB), University of Duisburg-Essen, Essen, Germany. ¹³Department of Immunodynamics, Institute of Experimental Immunology and Imaging, University Hospital Essen, Essen, Germany. ¹⁴Rudolf Schönheimer Institute of Biochemistry, Medical Faculty, University of Leipzig, Leipzig, Germany. ¹⁵Department of Nuclear Medicine, University Hospital Essen, University of Duisburg-Essen, Essen, Germany. ¹⁶Department of Dermatology and Allergology, Ludwig Maximilian University Munich, Munich, Germany. ¹⁷NCT West, Campus Essen and University Alliance Ruhr, Research Center One Health, University Duisburg-Essen, Essen, Germany. ✉e-mail: alexander.roesch@uk-essen.de



Extended Data Fig. 1 | See next page for caption.

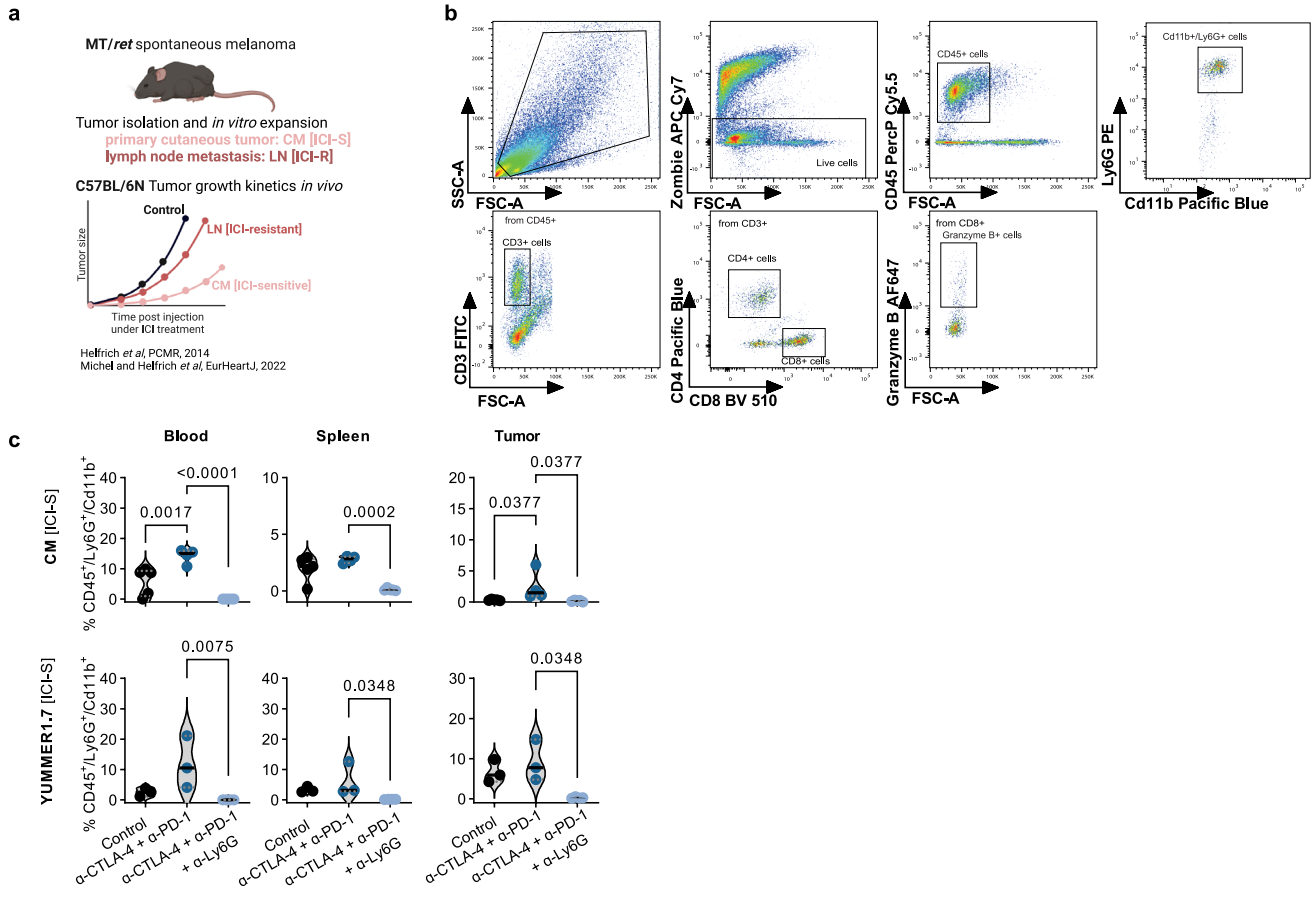
Extended Data Fig. 1 | The association between the IL-17A signaling and MAPK pathways. (a) Gene set enrichment analysis in the discovery cohort showing (left) the normalized enrichment scores in pathways according to significance level and the corresponding enrichment plot for IL-17 signaling pathway (right). (b) Volcano plot showing the difference in MAPK wt (n = 36 triple wt tumors) and MAPK mt (n = 120 tumors with BRAF/NRAS hotspot and NF1 mutated tumors) associated gene expression (log₂ values) and q-values (-log₁₀ adjusted p-values from multiple unpaired t-test with Benjamini, Krieger and Yekutieli test correction) in the discovery cohort. Each dot represents a gene; significant DEGs (q < 0.05) are shown in a color-coded manner (left). Bar plot showing the enrichment scores (-log₁₀ adjusted p-values, Benjamini–Hochberg corrected FDR) of functional pathways as defined by the Wiki, Reactome, and KEGG pathway databases (right). (c) Box and whiskers plots for gene expression of Th17/IL-17-inducing genes in the TCGA-SKCM cohort grouped according to BRAF status (n = 197 wt and n = 166 mt biologically independent tumors). Boxplot show the median (line) and interquartile ranges (Tukey whiskers that extend

to 1.5 × IQR); p-values represent Mann-Whitney U test. (d) Scatter dot plots for gene expression of Th17/IL-17-inducing genes in the MAPKi dataset (Long et al, Rizos et al, and Kakavand et al datasets: GSE61992, GSE50509, GSE99898 series combined) grouped according to sample collection time point (PRE: before, ON: during therapy). Dots represent biologically independent tissues (n = 47 ON, n = 11 PRE) and are color-coded according to dataset; shown is mean ± 95% CI; p-values are from unpaired t-test. (e) qPCR analysis of BRAF mt (WM9, WM983B, 451Lu) melanoma cells treated with 1 nM dabrafenib/0.2 nM trametinib vs. DMSO for 7 days. Bar plot shows mean ± SEM where single dots represent biologically independent cell lines; p-values are from unpaired t-test. Shown is one representative out of three independently performed experiments. All p-values are two-tailed. mt: mutant, wt: wild-type, GSEA: gene set enrichment analysis, FDR: false discovery rate, NES: normalized enrichment score, TCGA: The Cancer Genome Atlas, SKCM: Skin cutaneous melanoma, MAPKi: mitogen-activated protein kinase inhibitor, IQR: interquartile range.



Extended Data Fig. 2 | IL-17A supports anti-tumor effects of dual ICI in mouse melanoma. (a) Kaplan Meier plot related to Fig. 2a, showing survival of mice. p-values are from log rank test. (b) Extended immunostaining panel related to Fig. 2e showing IL-17A and CD4 positivity in the CM (BRAF wt, ICI-sensitive) mouse model. Corresponding scatter dot plots of immunostaining quantification (n = 5 random fields/whole tumor area normalized to DAPI; n = 2 biologically independent tumors/group). (c) Tumor growth kinetics of YUMM1.7 (BRAF mt, ICI-resistant) melanoma treated with IgG/H₂O (control,

n = 5), α -CTLA-4 + α -PD-1 (n = 4), α -CTLA-4 + α -PD-1 plus rm-IL-17A (n = 4) according to treatment schedule as depicted. Data points show mean + SEM, and p-values are from 1-way ANOVA with Holm-Sidak's multiple comparisons test. (d) Corresponding cytokine and chemokine concentrations as quantified by a multiplex cytokine array in endpoint serum samples (day 19). Bar plot shows n = 3 to 6 biologically independent samples/group. Data points show mean + SEM, and p-values are from unpaired t-test. All p-values are two-tailed.



Extended Data Fig. 3 | Experimental details of neutrophil *in vivo* experiments. (a) Schematic workflow for LC-MS/MS analysis. (b) Flow cytometry gating strategy. (c) Violin plots show the distribution of Ly6G⁺ neutrophils in blood, spleen, and tumor tissues of mice from Fig. 4a,b. p-values are from 1-way

ANOVA with Holm-Sidak's multiple comparisons test (top panels, CM model) and from Kruskal-Wallis test with Dunn's multiple comparisons test (bottom panels, YUMMER1.7 model). All p-values are two-tailed. LC-MS/MS: liquid chromatography-mass spectrometry/mass spectrometry.

Reporting Summary

Nature Portfolio wishes to improve the reproducibility of the work that we publish. This form provides structure for consistency and transparency in reporting. For further information on Nature Portfolio policies, see our [Editorial Policies](#) and the [Editorial Policy Checklist](#).

Statistics

For all statistical analyses, confirm that the following items are present in the figure legend, table legend, main text, or Methods section.

- | n/a | Confirmed |
|-------------------------------------|--|
| <input type="checkbox"/> | <input checked="" type="checkbox"/> The exact sample size (n) for each experimental group/condition, given as a discrete number and unit of measurement |
| <input type="checkbox"/> | <input checked="" type="checkbox"/> A statement on whether measurements were taken from distinct samples or whether the same sample was measured repeatedly |
| <input type="checkbox"/> | <input checked="" type="checkbox"/> The statistical test(s) used AND whether they are one- or two-sided
<i>Only common tests should be described solely by name; describe more complex techniques in the Methods section.</i> |
| <input checked="" type="checkbox"/> | <input type="checkbox"/> A description of all covariates tested |
| <input type="checkbox"/> | <input checked="" type="checkbox"/> A description of any assumptions or corrections, such as tests of normality and adjustment for multiple comparisons |
| <input type="checkbox"/> | <input checked="" type="checkbox"/> A full description of the statistical parameters including central tendency (e.g. means) or other basic estimates (e.g. regression coefficient) AND variation (e.g. standard deviation) or associated estimates of uncertainty (e.g. confidence intervals) |
| <input type="checkbox"/> | <input checked="" type="checkbox"/> For null hypothesis testing, the test statistic (e.g. F , t , r) with confidence intervals, effect sizes, degrees of freedom and P value noted
<i>Give P values as exact values whenever suitable.</i> |
| <input checked="" type="checkbox"/> | <input type="checkbox"/> For Bayesian analysis, information on the choice of priors and Markov chain Monte Carlo settings |
| <input checked="" type="checkbox"/> | <input type="checkbox"/> For hierarchical and complex designs, identification of the appropriate level for tests and full reporting of outcomes |
| <input type="checkbox"/> | <input checked="" type="checkbox"/> Estimates of effect sizes (e.g. Cohen's d , Pearson's r), indicating how they were calculated |

Our web collection on [statistics for biologists](#) contains articles on many of the points above.

Software and code

Policy information about [availability of computer code](#)

Data collection The TCGA SKCM gene expression data was retrieved from the GDAC Firehose (<http://gdac.broadinstitute.org>) site.

Data analysis The following softwares were used: GraphPad Prism v.9.5.1 for statistical testing and visualization, Partek Flow v.10.0 for microarray data processing and count normalization, ImageJ v.1.50i for image quantification, R v.3.6.1 for RNA-Seq data kallisto normalization, DeSeq2 v.3.17 for normalization, StepOnePlus v.2.3 for qRT-PCR data analyses, ZEN v.3.1 (blue edition) for fluorescent image processing, FlowJo v.10.8.1 for flow cytometry data, X-tile v.3.6.1 for optimal cutpoint determination for survival curves, WebGestalt v.2019 (<http://www.webgestalt.org/>) for pathway and GSEA analysis, LegendPlex analysis software v. 2021. 07.01 (<https://legendplex.qognit.com/>) for MFI determination of cytokine arrays, STRING v.11.5 database (<https://string-db.org/>) for protein-protein interaction, xCell v.2020 (<https://xcell.ucsf.edu/>) for immune deconvolution. Hedges' g was calculated after the formula by Hedges and Olkin (Hedges, L. V. & Olkin, I. 1985: Statistical methods for meta-analysis. Orlando, FL: Academic Press).

For manuscripts utilizing custom algorithms or software that are central to the research but not yet described in published literature, software must be made available to editors and reviewers. We strongly encourage code deposition in a community repository (e.g. GitHub). See the Nature Portfolio [guidelines for submitting code & software](#) for further information.

Data

Policy information about [availability of data](#)

All manuscripts must include a [data availability statement](#). This statement should provide the following information, where applicable:

- Accession codes, unique identifiers, or web links for publicly available datasets
- A description of any restrictions on data availability
- For clinical datasets or third party data, please ensure that the statement adheres to our [policy](#)

Previously published RNA-Seq data that were re-analysed here are available under accession code phs000452.v3.p1 [Liu et al 17]; phs000452.v2.p1 [Van Allen et al ref. 16]; PRJEB23709 [Gide et al ref. 18]; GSE91061 [Riaz et al ref. 19]; GSE61992 [Long et al ref. 13]; GSE50509 [Rizos et al ref. 14]; GSE99898 [Kakavand et al ref. 15]. Data from the discovery cohort [Brase et al ref. 9] was obtained directly from the authors with permission of Novartis. The human melanoma RNA-Seq data were derived from the TCGA Research Network: <http://cancergenome.nih.gov/>. Source data for Fig. 1a, 3e, and Extended Data Fig. 1a (KEGG database, release no. 99) and 1b have been provided as Source Data files. All other data supporting the findings of this study are available from the corresponding author on reasonable request.

Human research participants

Policy information about [studies involving human research participants and Sex and Gender in Research](#).

Reporting on sex and gender

All human research participants were included in the study regardless of sex and gender. In the total plasma/serum cohort (Figure 4, S4) the sex distribution was 58% males and 42% females.

Population characteristics

Plasma cohort: n = 70 metastatic melanoma patients who received first-line ipilimumab plus nivolumab (median age 60 yrs; n = 45 male, n = 25 female; n = 27 BRAF V600 positive, n = 43 BRAF V600 negative) and n = 51 metastatic melanoma patients who received first-line nivolumab or pembrolizumab (median age 71 yrs; n = 28 male, n = 23 female; n = 11 BRAF V600 positive, n = 38 BRAF V600 negative, n = 2 unknown) were included in this study.
 Serum cohort: n = 45 metastatic melanoma patients who received ipilimumab plus nivolumab (median age 62 yrs; n = 29 male, n = 16 female; n = 17 BRAF V600 positive, n = 25 BRAF V600 negative, n = 3 unknown) and n = 44 metastatic melanoma patients who received nivolumab or pembrolizumab (median age 71 yrs; n = 20 male, n = 24 female; n = 12 BRAF V600 positive, n = 31 BRAF V600 negative, n = 1 unknown) were included in this study.
 Patient-derived tumor fragments (PDTFs): Clinical data of this cohort are described by the original authors [references 23,24]. This study also included analysis of previously published melanoma cohorts [as described in section Software and code/Data collection]. Clinical data of these cohorts are described by the authors in their respective publications [references 14-20].

Recruitment

The samples analyzed in this study were obtained through biobanking procedures as outlined below. Patients were not recruited specifically for this study. Patients did not receive compensation.
 All patients who received immunotherapy and consented to institutional biobanking procedures were identified by treating physicians at the respective institutions.
 Patients in the plasma cohort were treated at the Department of Dermatology of the University Hospital Essen in Germany in standard-of-care or clinical trial settings.
 Patients in the serum cohort were treated at dermatology departments at the University Hospital of Tübingen (Germany), University Medical Center Mannheim (Germany), Kantonsspital St. Gallen (Switzerland), and University Hospital Essen (Germany) in standard-of-care or clinical trial settings.
 PDTFs: Human resected tumor samples were collected from patients with melanoma undergoing surgical treatment at the Netherlands Cancer Institute (NKI-AVL).

Ethics oversight

Plasma and serum Essen cohorts: human biological samples and related data were provided by the Westdeutsche Biobank Essen (WBE/SCABIO) and approval was provided by the University Hospital Essen, University of Duisburg-Essen, Essen, Germany (approval no. 11-4715, 21-9985-BO) according to institutional informed consent procedures.
 Additional serum cohorts: sample were collected in compliance with the ethical regulations of the respective institutions' and approval was provided by the Ethical committee of Tübingen University Medical Center (490/2014 B01, 089/2021A), the Ethical committee II of Heidelberg University (2010-318N-MA) and Ethikkommission Ostschweiz (EKOS 16/079).
 PDTFs: resected tumor samples were collected from patients with melanoma undergoing surgical treatment at the Netherlands Cancer Institute (NKI-AVL), The Netherlands. The study was approved by the institutional review board of the NKI-AVL (CFMPB484) and executed in compliance with the ethical regulations. All patients consented to the research usage of material not required for diagnostics via prior informed consent.

Note that full information on the approval of the study protocol must also be provided in the manuscript.

Field-specific reporting

Please select the one below that is the best fit for your research. If you are not sure, read the appropriate sections before making your selection.

- Life sciences Behavioural & social sciences Ecological, evolutionary & environmental sciences

For a reference copy of the document with all sections, see [nature.com/documents/nr-reporting-summary-flat.pdf](https://www.nature.com/documents/nr-reporting-summary-flat.pdf)

Life sciences study design

All studies must disclose on these points even when the disclosure is negative.

Sample size	<p>Human plasma and serum samples: the melanoma patient cohort size calculation for cytokine assays was based on power analysis using Chi-squared statistic assuming a relative risk of 2.0 between outcome positive and outcome negative proportions (type I/II errors at 0.05 and 0.20, respectively).</p> <p>Mice: group size was determined based on data from preliminary experiments to detect >20% effect between groups (type I/II errors at 0.05 and 0.20, respectively). In all experiments a minimum of n = 4 mice were used to ensure a balance between statistical needs and animal welfare.</p> <p>Sample size was calculated on https://sample-size.net/.</p> <p>For all other experiments, including in vitro experiments, no sample size calculation was performed, however, reproducibility of the method has been demonstrated on minimum three biologically independent samples. In addition, successful replication experiments were considered enough to demonstrate sufficient sample size to identify consistent differences between groups.</p>
Data exclusions	<p>Public gene expression profiling datasets: only the samples with available baseline gene expression, mutational data and clinical annotation were analyzed.</p> <p>In the TCGA SKCM cohort, only one sample/patient was analyzed for survival analysis (in case of patients who donated multiple samples).</p> <p>In the MAPKi datasets (GSE61992, GSE50509, GSE99898) where replicate tumors of the same tumor lesions were profiled, we analyzed the sample with higher expression value (in general there were minor expression differences for replicate tumors). Exact patient numbers are given in Materials and Methods and reflected in figures (e.g. in Kaplan Meier plots) or in figure legends (Figure 1f-l).</p> <p>Murine cytokine measurements: serum samples with significant hemolysis from red blood cells and samples which yielded less than 50 microliter serum (amount needed for ELISA assay) were not analyzed for cytokine levels (Figure 2b, Extended Figure 2d).</p> <p>Flow cytometry: each murine tumor sample was divided equally to run two staining protocols (lymphocyte and myeloid panels, see below under Flow Cytometry section) simultaneously, where n=1 tumor (out of n = 5) yielded in less than 20,000 viable cells, thus could not be included in the lymphocyte panel (Figure 4c).</p>
Replication	<p>Individual dots represent individual patients/mice/cell lines in figures and these are described in the figure legends.</p> <p>In all in vitro experiments technical replicates were set up (n = 2 to 10; see list below) and were reproduced independently at least twice. All attempts and replication were successful.</p> <p>RT-qPCR: minimum n = 3 biological replicates, minimum n = 2 to 3 technical replicates were set up.</p> <p>IF staining and quantification: n = 2 mouse tumors (biological replicates) was used for IHC. Shown in Figure 2g and Extended Figure 2b is 1 representative tumor/treatment group. Consecutive tissue slices were stained for the three different antibody panels. For quantification n = 10 random fields/whole tumor area was digitally quantified.</p> <p>Cytokine assays (ELISA and LegendPlex): technical replicates (n = 2) were set up following manufacturer's instruction. Samples derived from individual patients (total n = 210), or mice (minimum n = 4 mice/group/experiment) were regarded as biological replicates.</p> <p>In vivo experiments:</p> <p>In general, treatment effects were tested using two independent mouse models. Where possible, different mouse strains were used. The results were reproducible between mouse models and strains, these are detailed below:</p> <p>Figure 2: using the CM mouse model in C57BL/6N mice, the same treatment groups and doses were set up in two independent experiments (Figure 2a and Figure 2g for long or short-term growth kinetics). Figure 2a was replicated using an independent mouse melanoma model (YUMM1.7) in C57BL/6J mice (Extended Figure 2c).</p> <p>Figure 4: the same treatment groups and doses were set up in two independent experiments using two independent mouse models (CM and YUMMER1.7) in C57BL/6N mice (Figure 4a and 4b).</p>
Randomization	<p>In vitro experiments: Mouse tumors were sectioned and subjected to IF staining in a consistent manner without specific allocation. When quantifying the images for specific marker expression, microscopy fields to be quantified were randomly chosen adhering to the same area size within the whole tumor area. Background correction was done separately for each marker and results were normalized to their respective DAPI controls.</p> <p>For other in vitro experiments, no relevant differing covariates could be identified, thus there was no need for randomization. All samples were processed/measured in a consistent manner.</p> <p>In vivo experiments: mice were randomly grouped in different cages. Within each cage, mice were randomized for different ICI therapies. When tumors became palpable (typically on day 5), ICI receiving mice were further randomized to different combination therapies. Patient samples were also not randomized since the clinical variable (e.g. genotype or response to therapy) analyzed determined the group. Data was not randomized.</p>
Blinding	<p>In vitro experiments: human cytokine analyses (ELISA and LegendPlex multiplex cytokine array) on plasma and serum samples were done in a blinded fashion. Investigators who performed cytokine measurement were blinded to clinical response data which was provided by independent medical researchers after completion of sample measurement.</p> <p>In vivo experiments: complete blinding was not possible, even though therapy administration was done following eartags. However, during tumor size measurement the investigator who measured had no knowledge of the treatment group and cage number which was picked by a second assisting investigator.</p> <p>For all other experiments (in vitro, bioinformatics) blinding was not possible since the person who performed the experiment had to have knowledge of the condition applied (i.e. treatment with drug vs control) or group to be analyzed. However, when possible, a second researcher confirmed the results.</p>

Reporting for specific materials, systems and methods

We require information from authors about some types of materials, experimental systems and methods used in many studies. Here, indicate whether each material, system or method listed is relevant to your study. If you are not sure if a list item applies to your research, read the appropriate section before selecting a response.

Materials & experimental systems

n/a	Involved in the study
<input type="checkbox"/>	<input checked="" type="checkbox"/> Antibodies
<input type="checkbox"/>	<input checked="" type="checkbox"/> Eukaryotic cell lines
<input checked="" type="checkbox"/>	<input type="checkbox"/> Palaeontology and archaeology
<input type="checkbox"/>	<input checked="" type="checkbox"/> Animals and other organisms
<input checked="" type="checkbox"/>	<input type="checkbox"/> Clinical data
<input checked="" type="checkbox"/>	<input type="checkbox"/> Dual use research of concern

Methods

n/a	Involved in the study
<input checked="" type="checkbox"/>	<input type="checkbox"/> ChIP-seq
<input type="checkbox"/>	<input checked="" type="checkbox"/> Flow cytometry
<input checked="" type="checkbox"/>	<input type="checkbox"/> MRI-based neuroimaging

Antibodies

Antibodies used

IF:
 Melan A clone EPR20380, Abcam #ab210546, 1:1000
 Ly6G clone RB6-8C5, BioLegend #108401, 1:100
 CD8a clone C8/144B, BioLegend #372902, 1:100
 CD11c clone N418, BioLegend #117301, 1:100
 CD4 clone RM4-5, BioLegend # 100505, 1:100
 IL-17A clone TC11-18H10.1, BioLegend # 506901, 1:100
 Peroxidase AffiniPure Mouse Anti-Rat IgG (H+L), Dianova, #212-035-082, 1:1000
 Peroxidase AffiniPure Goat Anti-Armenian Hamster IgG (H+L), Dianova, #127-035-160, 1:1000

In vivo:
 anti-mouse CTLA-4 clone 9D9, BioXCell #BE0164, 8 mg/kg body weight
 anti-mouse PD-1 clone RMP1-14, BioXCell #BE0146, 10 mg/kg body weight
 IgG2a isotype control clone 2A3, BioXCell #BE0089, 10 mg/kg body weight
 Ultra-LEAF™ purified anti-mouse IL-17A antibody clone TC11-18H10.1, BioLegend #506946, 4 mg/kg body weight
 anti-mouse Ly6G clone 1A8, Leinco Technologies #L280, 4 mg/kg body weight
 IL-17A mouse recombinant, Prospec #CCYT-378, 0.01 mg/kg body weight

Ex vivo:
 anti-human IL-17A clone BL168, BioLegend #512302, 10 µg/mL final concentration
 anti- PD-1: Nivolumab, Bristol-Myers Squibb #BMS-936558, 10 µg/mL final concentration
 anti CTLA-4: Ipilimumab, Bristol-Myers Squibb #BMS-986288, 10 µg/mL final concentration

Flow cytometry:
 Lymphocyte panel:
 anti-CD45 PerCP Cy5.5, clone 30-F11, BioLegend #103131, 1:100
 anti-CD3 FITC, clone 17A2, BioLegend 3100203, 1:100
 anti-CD4 Pacific Blue, clone RM4-5, BioLegend #100534, 1:100
 anti-CD8a Bright Violet 510, clone 53-6.7, BioLegend #100752, 1:100
 anti-Granzyme B Alexa Fluor 647, BioLegend #515405, clone GB11, 1:100
 Myeloid panel:
 anti-CD45 PerCP Cy5.5, clone 30-F11, BioLegend #103131, 1:100
 anti-CD11b Pacific Blue, clone M1/70, BioLegend #101223, 1:100
 anti-CD11c Alexa Fluor 488, clone N418, BioLegend #117313, 1:100
 anti-Ly6C Alexa Fluor 647, clone HK1.4, BioLegend #128009, 1:100
 and anti-Ly6G PE, clone 1A8, BioLegend #127607, 1:100

Validation

All antibodies were purchased from established companies with well-documented specificities and experimental applications (paper references, data sheets). All antibodies were validated by the supplier.

Website, Host species, Reactivity, Suitability

IF:
<https://www.biolegend.com/en-us/products/purified-anti-mouse-ly-6g-ly-6c-gr-1-antibody-462> Rat Mouse IF, Flow Cyt., WB, IHC, IP
<https://www.biolegend.com/en-us/products/purified-anti-human-cd8a-antibody-13983> Mouse Human, Mouse, Rat IHC-P, IHC-F, WB
<https://www.biolegend.com/en-us/products/purified-anti-mouse-cd11c-antibody-1817> Armenian Hamster Mouse IF, Flow Cyt., IHC, IP, CyTOF
<https://www.biolegend.com/en-us/products/purified-anti-mouse-cd4-antibody-484> Rat Mouse IF, Flow Cyt., IHC, CyTOF
<https://www.biolegend.com/en-us/products/purified-anti-mouse-il-17a-antibody-1634> Rat Mouse ELISA, CyTOF
<https://www.jacksonimmuno.com/catalog/products/212-035-082>, Mouse Rat WB, IHC, ELISA
<https://www.jacksonimmuno.com/catalog/products/127-035-160>, Goat Hamster WB, IHC, ELISA

In vivo:	<p>https://bioxcell.com/invivomab-anti-mouse-ctla-4-cd152-be0164 Unkown Mouse In vivo, WB</p> <p>https://bioxcell.com/invivomab-anti-mouse-pd-1-cd279-be0146 Syrian Hamster Mouse In vivo</p> <p>https://bioxcell.com/invivomab-rat-igg2a-isotype-control-anti-trinitrophenol-be0089 Rat In vivo</p> <p>https://www.biolegend.com/en-us/products/ultra-leaf-purified-anti-mouse-il-17a-antibody-16817 Rat Mouse In vivo</p> <p>https://www.leinco.com/p/anti-mouse-ly-6g-purified-functional-grade-gold/ Rat Mouse In vivo, CyTOF,FC,IHC FF,WB</p> <p>https://www.prospecbio.com/il-17_mouse</p>
Ex vivo:	<p>https://www.biolegend.com/en-us/products/purified-anti-human-il-17a-antibody-4442 Mouse Human ICFC,IF,Flow Cyt.</p> <p>https://bioxcell.com/invivosim-anti-human-pd-1-nivolumab-biosimilar Human Flow Cyt.,WB,IHC</p> <p>https://bioxcell.com/invivosim-anti-human-ctla-4-ipilimumab-biosimilar Human Flow Cyt.,WB,ELISA</p>
FACS:	<p>https://www.biolegend.com/en-us/products/percp-cyanine5-5-anti-mouse-cd45-antibody-4264 Rat Mouse Flow Cyt.</p> <p>https://www.biolegend.com/en-us/products/fitc-anti-mouse-cd3-antibody-45 Rat Mouse Flow Cyt.</p> <p>https://www.biolegend.com/en-us/products/pacific-blue-anti-mouse-cd4-antibody-2855 Rat Mouse Flow Cyt.</p> <p>https://www.biolegend.com/en-us/products/brilliant-violet-510-anti-mouse-cd8a-antibody-7992 Rat Mouse Flow Cyt.</p> <p>https://www.biolegend.com/en-us/products/alexa-fluor-647-anti-human-mouse-granzyme-b-antibody-6067 Mouse Human,Mouse Flow Cyt.</p>
	<p>https://www.biolegend.com/en-us/products/percp-cyanine5-5-anti-mouse-cd45-antibody-4264 Rat Mouse Flow Cyt.</p> <p>https://www.biolegend.com/en-us/products/pacific-blue-anti-mouse-human-cd11b-antibody-3863 Rat Mouse, Human, Cynomolgus, Rhesus Flow Cyt.</p> <p>https://www.biolegend.com/en-us/products/alexa-fluor-488-anti-mouse-cd11c-antibody-2702 Armenian Hamster Mouse Flow Cyt.</p> <p>https://www.biolegend.com/en-us/products/alexa-fluor-647-anti-mouse-ly-6c-antibody-4897 Rat Mouse Flow Cyt.</p> <p>https://www.biolegend.com/en-us/products/pe-anti-mouse-ly-6g-antibody-4777 Rat Mouse Flow Cyt.</p>

Eukaryotic cell lines

Policy information about [cell lines and Sex and Gender in Research](#)

Cell line source(s)	The human melanoma cell lines WM983B, 451Lu, and WM9 were obtained from the Wistar Institute. The mouse melanoma cell lines derived from the MT/ret spontaneous melanoma model (CM and LN, [reference 20]) were obtained from Prof. Iris Helfrich (University Hospital Essen, Germany). The mouse melanoma cell line YUMM1.7 (CRL-3362) was purchased from ATCC and the YUMMER1.7 (clone D4) cell line was purchased from Merck.
Authentication	Cell line identity was confirmed by PCR-based DNA fingerprinting at the Department of Pathology of the University Hospital Essen.
Mycoplasma contamination	All cell lines were regularly monitored and tested negative for mycoplasma contamination.
Commonly misidentified lines (See ICLAC register)	No misidentified cell line was used in this study.

Animals and other research organisms

Policy information about [studies involving animals; ARRIVE guidelines](#) recommended for reporting animal research, and [Sex and Gender in Research](#)

Laboratory animals	8 weeks old female C57BL/6N or C57BL/6J mice were used for experiments. All mice were housed in rooms maintained at a constant temperature of 22°C and 45-65% humidity with a 12 hour light cycle. Animals were allowed food and water ad libitum.
Wild animals	The study did not involve wild animals.
Reporting on sex	Female mice were used in this study due to mitigated immune response to ICI therapies in male mice (according to several published reports (references: doi.org/10.3181/00379727-127-32768 , doi.org/10.1016/j.bb.2021.08.225))
Field-collected samples	The study did not involve field-collected samples.
Ethics oversight	All animal experiments were performed in accordance with institutional and national guidelines and regulations. Ethical approval was provided by the local state authority Landesamt für Natur, Umwelt und Verbraucherschutz Nordrhein-Westfalen – LANUV NRW in compliance with the German animal protection law (reference number 81-02.04.2018.A202).

Note that full information on the approval of the study protocol must also be provided in the manuscript.

Flow Cytometry

Plots

Confirm that:

- The axis labels state the marker and fluorochrome used (e.g. CD4-FITC).
- The axis scales are clearly visible. Include numbers along axes only for bottom left plot of group (a 'group' is an analysis of identical markers).
- All plots are contour plots with outliers or pseudocolor plots.
- A numerical value for number of cells or percentage (with statistics) is provided.

Methodology

Sample preparation

LegendPlex:

Manufacturer's recommended protocol was followed. In brief, plasma samples were incubated with APC beads conjugated with the antibody of interest (bead panels are specified in the Materials and Methods). Afterwards biotinylated detection antibodies (SA-PE) were applied.

Flow cytometry of murine samples:

Tissues were digested using the Mouse Tumor Dissociation Kit (Miltenyi) on the GentleMACS device (Miltenyi) according to the manufacturer's instruction. Red blood cell lysis buffer (BioLegend) was used to remove red blood cells. After washing with PBS, cells were incubated with TruStain fcX anti mouse CD16/32receptor blocking agent (BioLegend) diluted in Cell Staining Buffer (BioLegend) for 20 min at 4°C. After washing Zombie NIR cell viability dye (1:2000, Biolegend) was added and incubated for 20 min at 4°C. To assess immune cell composition the following antibodies were added for 30 min at 4°C for lymphocytes: anti-CD45 PerCP Cy5.5 (30-F11, 1:100), anti-CD3 FITC (17A2, 1:100), anti-CD4 PB (RM4-5, 1:100) anti-CD8a BV 510 (53-6.7, 1:100), anti-Granzyme B AF 647(GB11, 1:100); for macrophages: anti-CD45 PerCP Cy5.5 (30-F11, 1:100), anti-CD11B PB (M1/70, 1:100), anti-CD11C AF 488 (N418, 1:100), anti-Ly6C AF 647 (HK1.4, 1:100), and anti-Ly6G PE (1A8, 1:100), all from Biolegend. Granzyme B was added after surface staining was complete, and after a fixation/permeabilization (Fixation Buffer: BioLegend Cat #420001, 10x Intracellular Staining Perm Wash Buffer, BioLegend Cat #421002). Subsequently, samples were washed twice before data acquisition on BD Aria III flow cytometer. Gating strategy is shown in Extended Figure 3b.

Instrument

FACSAria™ III (BD) machine with nozzle size 70 µm was used.

Software

LegendPlex:

Mean fluorescence intensity (MFI) values were recorded from the LEGENDplex™ analysis software (version 2021. 07.01, <https://legendplex.qognit.com>) and cytokine concentrations (pg/ml) were interpolated from 5-parameter logistic (5PL) non-linear curve model using separate standard curve for each cytokine.

Flow cytometry of murine samples:

Samples acquisition was done on FACS Diva v.9.0.1. software (BD) and analysis was carried out in FlowJo v. 10.8.1.

Cell population abundance

MACS sorted T cell and neutrophil cellular abundance was confirmed by flow cytometry and purity above 90% was accepted for downstream applications.

Gating strategy

Cells were gated on forward and side scatter parameters (FSC/SSC), then dead cells (Zombie APC Cy7 positive) were excluded. Immune cells were gated based on CD45 positivity, then lymphocytes were subsequently gated on CD3, then on CD4 or CD8 positive populations. Granzyme B was gated on CD8 positive cells. Neutrophils were gated from the CD45 positive population based on Cd11b/Ly6G double positive cells.

- Tick this box to confirm that a figure exemplifying the gating strategy is provided in the Supplementary Information.